Quantum Electronics **36** (10) 895–917 (2006)

REVIEW

PACS numbers: 42.62.Fi, 78.47.+p, 74.25.Gz, 78.20.Bh
DOI: 10.1070/QE2006v036n10ABEH013235

Spectral, temporal and temperature features of the nonlinear response of high-temperature superconductors in transient nonlinear spectroscopy

Yu.V. Bobyrev, V.M. Petnikova, K.V. Rudenko, V.V. Shuvalov

***Abstract*. It is shown that basic properties of the nonlinear response of high-temperature superconductors (HTSCs) observed in femtosecond and picosecond pump–probe experiments at high and low pump levels in various variants of the pump–probe spectroscopy, including one- and two-photon excited-state probing, can be interpreted by using two assumptions. The spectral and temperature properties of the HTSC response at low pump levels can be explained taking into account the contributions from interband electronic transitions to the dielectric constant. At the same time, drastic variations in the HTSC response kinetics (temporal features) observed at high pump levels (for a typical pump pulse energy of $\sim 10^{-7}$ J in a focal spot of diameter 150 μm) can be explained by assuming the existence of a 'frozen' (metastable) energy gap in the electronic spectrum of a HTSC. In this case, all the conditions required for the interpretation of a drastic decrease in the relaxation rate of a nonlinear response (degeneracy) are realised due to the specific distribution of the electronic state density immediately after the formation of the energy gap in the electronic spectrum of the HTSC.**

Keywords: *nonlinear HTSC spectroscopy, spectral, temporal and temperature features of a nonlinear response, metastable energy gap, interband electronic transitions, degeneracy of electronic states.*

1. Introduction

The development of methods for generating ultrashort laser pulses has stimulated the studies of processes of ultrafast relaxation of photoexcitations in metals [1–11] and low-temperature [12–16] and high-temperature [17–34] superconductors (LTSC and HTSC). Such experiments attract interest, in particular, in connection with the outlook for elaborating ultrafast and supersensitive HTSC bolometers [17, 23]. However, it is more important that such investigations can give new information shedding light on the physics of the high-temperature superconductivity phenomenon itself.

Yu.V. Bobyrev, V.M. Petnikova, K.V. Rudenko, V.V. Shuvalov
International Laser Center, M.V. Lomonosov Moscow State University, Vorob'evy gory, 119992 Moscow, Russia

Received 10 April 2006
Kvantovaya Elektronika **36** (10) 895–917 (2006)
Translated by M.N. Sapozhnikov

Almost all experiments of this type use the classical version of the pump–probe spectroscopy (Fig. 1) for studying the dependence of a change ΔR in the reflection coefficient [and (or) transmission coefficient ΔT] of a sample on the delay time τ of a short probe pulse with respect to the arrival time of a short pump pulse (impact excitation) [18–22]. The obtained data are usually processed by means of standard expression [34]

$$\Delta R(\tau) \propto A(T)\left\{H(\tau)\left[1-\exp\left(-\frac{\tau}{\tau_{\rm th}}\right)\right]\exp\left(-\frac{\tau}{\tau_{\rm r}}\right)\right\}, \quad (1)$$

where $A(T)$ is the temperature-dependent transient response amplitude; $H(\tau)$ is the Heaviside step function; and $\tau_{\rm th}$ and $\tau_{\rm r}$ are the thermalisation and relaxation times of optically excited carriers (see below). Other methods of nonlinear spectroscopy such as stationary or transient modifications of biharmonic pumping (BP) [9, 25, 26], degenerate four-photon spectroscopy (DFPS) [10, 11] (Fig. 1), terahertz spectroscopy [27–29] or hybrid methods (optical excitation and recording of an electric response) [16, 17, 23, 24] are used rather rarely. In all these cases, other (most often spectral) properties of the nonlinear response are mainly studied [35–37]. However, the results of these experiments are also very important because all the data obtained must be interpreted within the framework of a unified model.

It was assumed until recently that the basic properties of processes proceeding under transient conditions are well

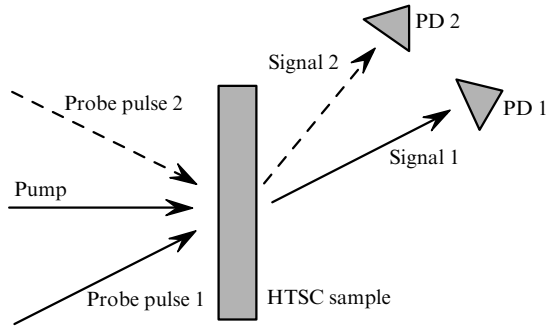

Figure 1. Scheme of the experiment with one-photon (spectrochronography) and two-photon (BP and DFPS methods) probing of the kinetics of variations induced by the pump pulse in a HTSC. Either one probe pulse 1 (whose transmission is measured with a PD-1 photodetector) or two probe pulses 1 and 2 coincident in time are used (the self-diffraction signal of probe pulses 1 and 2 is detected with a PD-2 photodetector).

known. After impact excitation, free carriers are first thermalised rapidly ($\tau_{th} < 10$ fs for the 'hot' electron energy $E_e \sim 1$ eV [38, 39]) during electron–electron (e–e) scattering. In this case, their energy distribution function $f(E_e)$ returns to the Fermi–Dirac distribution $f_F(E_e; T_e)$ with the electron energy T_e, which differs both from the initial temperature T_0 of a sample and the temperature T_p of its phonon subsystem (lattice) [40]. However, it was found that the thermalisation time was $\tau_{th} \sim 0.5$ ps even in elementary metals (Cu, Ag, Au, etc.) [5, 6, 40], which was attributed to restrictions imposed by the Fermi–Dirac statistics on the space of electronic states during e–e scattering. Moreover, the experiment did not reveal the dependence $\tau_{th} \propto T^{-2}$ predicted theoretically. This was explained by the fact that the sample temperature in experiments was not low enough [1–7, 41].

At the second stage, thermalised carriers are cooled (T_e decreases) due to electron–phonon (e–p) scattering during the time τ_r. This $T_e \to T_p$ process was first described within the framework of the so-called two-temperature model [42], which predicts for elementary metals the dependences $\tau_r \propto T$ for $T \geqslant T_D/5$ and $\tau_r \propto T^{-3}$ for $T \ll T_D/5$, where T_D is the Debye temperature [7, 41, 43–45]. However, the experiments did not reveal any substantial increase in τ_r in the region $T \ll T_D/5$, which was again explained by the restrictions imposed on the space of electronic states during low-temperature scattering [1–7]. This interpretation was confirmed, at first glance, by experiments with LTSCs and HTSCs [13–15, 17, 19, 30] in which the values of τ_{th} and τ_r drastically increased in the vicinity of the superconducting phase-transition point ($T_0 \simeq T_c$). It is such a behaviour of τ_{th} and τ_r that was predicted theoretically [12, 46–48] because simultaneously with the formation of the energy (superconducting) gap in the electronic spectrum, the corresponding restrictions also become considerably more rigid.

Experiments showed that the value of τ_r in LTSCs changed approximately by five times when T_0 was varied from 0.980 to $0.995T_c$ [15, 49–51]. This is consistent in principle with theoretical predictions [15, 51], according to which at low temperatures and a low excitation level, $\tau_r \propto \exp(\Delta/k_B T_c)$, where Δ is the energy gap in the electronic spectrum and k_B is the Boltzmann constant. The value of τ_r in a HTSC changed somewhat smaller on passing the point $T_0 \simeq T_c$ (Fig. 2a), approximately by a factor of 2–3 [52]. It was found that at a considerable distance from the peak of τ_r (point $T_0 \simeq T_c$), the relaxation time again increased with decreasing T_0 [31, 33], the increase being described by the law $\tau_r \propto T^{-3}$ [33, 53]. No reasonable explanation of this fact was proposed. A similar result was obtained in experiments with heavy fermion metals $YbXCu_4$ (where X = Ag, Cd, In) for which, unlike nonmagnetic $LuXCu_4$ compounds, the value of τ_r increased by more than two orders of magnitude for T_0 below the Kondo temperature [41].

That why paper [34], in which a substantially different result was obtained after a drastic decrease in the pump energy for a number of cuprates ($La_{2-\delta}Sr_\delta CuO_4$, $Bi_2Sr_2CuO_{6+\delta}$, doped La, and $Bi_2Sr_2CaCuO_{8+\delta}$), proved to be unexpected. It was shown that $\tau_r \propto T^{-3\pm0.5}$ for all these cuprates and τ_r begins to increase already in the

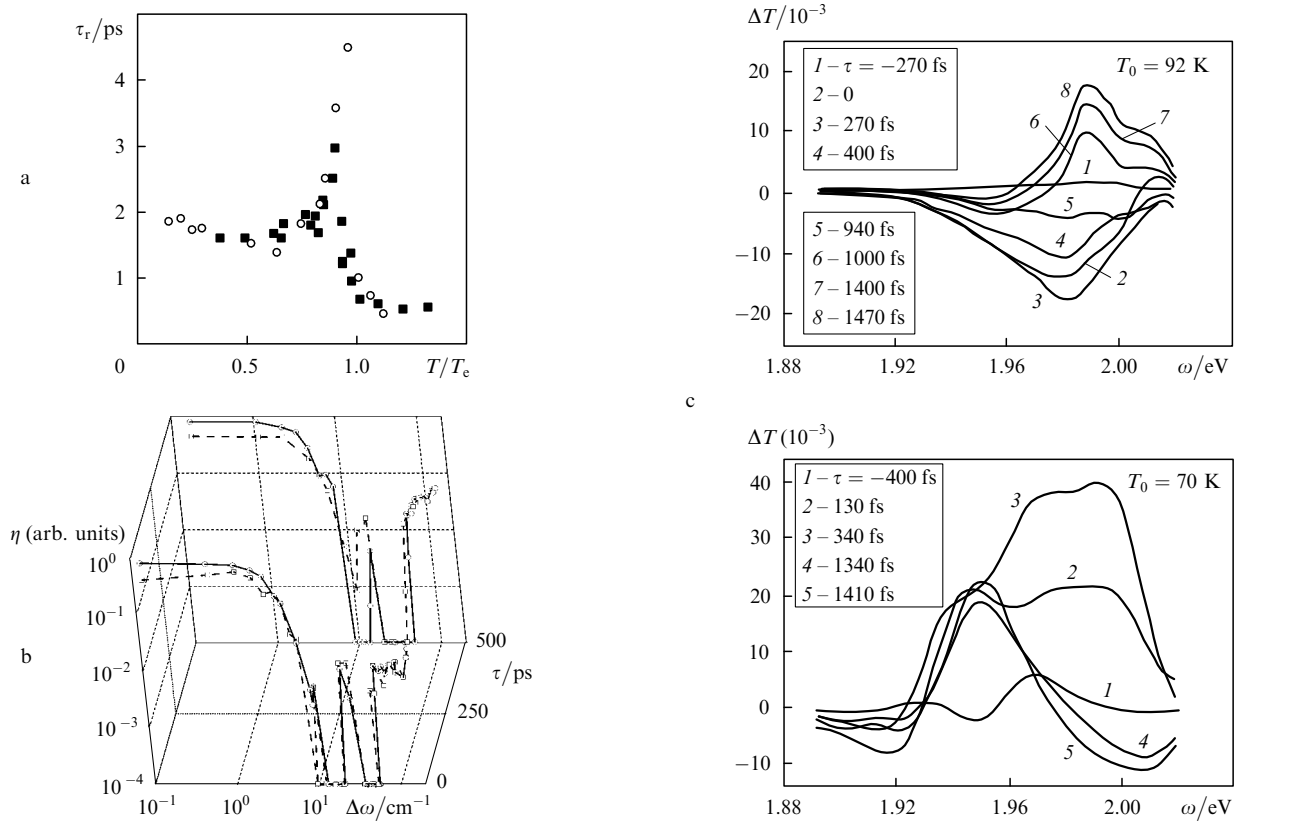

Figure 2. Experimental data for $YBa_2Cu_3O_{7-\delta}$: dependences $\tau_r(T/T_c)$ from [19] (squares) and [52] (circles) (a); dependences of the self-diffraction efficiency η on the frequency detuning $\Delta\omega$ of the BP components for $\tau = 0$ and 500 ps in the absence (solid curve) and presence (dashed curve) of the pump pulse [25] (b) and the dependence of ΔT on the probe-pulse frequency ω for different τ and $T_0 = 92$ and 70 K [22, 47] (c).

'normal' metal phase (for $T_0 > T_c$), while all the features of the behaviour of τ_r in the vicinity of the point of phase transition $T_0 \simeq T_c$ do take place, however, only at high excitation levels when a sample should almost instantly 'forget' information about its initial state (about its initial temperature T_0). Moreover, these features became more distinct with increasing the pump energy. The authors of [34] argue that, taking into account the data presented in [31–33, 53–55], the relaxation time τ_r in $YBa_2Cu_3O_{7-\delta}$, $Bi_2Sr_2CuO_{6+\delta}$, $Bi_2Sr_2CaCu_2O_{8+\delta}$, $La_{2-\delta}Sr_\delta CuO_4$, $Tl_2Ba_2CuO_{6+\delta}$, and $HgBa_2Ca_2Cu_3O_{8+\delta}$ behaves similarly. Note that control experiments with metal (Au) films revealed no substantial changes in τ_r in the temperature range from 10 to 280 K [34].

A quite unexpected result was also obtained in experiments on picosecond ($\sim$ 20-ps pulses) two-photon probing of the kinetics of the electronic spectrum of superconducting $YBa_2Cu_3O_{7-\delta}$ samples preliminary excited by a 20-ps pump pulse [25]. It was found that, despite a significant change in the temperature (by $\sim 20-40$ K) of an initially superconducting sample ($T_0 \simeq 80$ K) caused by pumping, all the features of the presence of the energy gap in its electronic spectrum were preserved at probe-pulse delays up to 1 ns [56, 57] (Fig. 2b). Because it is well known that superconductivity should disappear under such conditions during the time ~ 1 ps [23], this fact was not explained in [25]. Taking into account that the nonlinear response of HTSCs in the optical range is usually attributed to absorption by free carriers [34], rather drastic spectral variations in the amplitude $\Delta R(\lambda)$ and $\Delta T(\lambda)$ observed in experiments when the probe-pulse wavelength λ was different from the pump-pulse wavelength λ_p can be also attributed to the known anomalies of the nonlinear response (Fig. 2c) [22, 47].

Our paper is mainly of the review type and its aim is to explain consistently the spectral, temporal and temperature features of the nonlinear HTSC response, including all the above-mentioned anomalies observed by the methods of transient (femtosecond and picosecond) nonlinear spectroscopy. Below, we will use two assumptions for this purpose. First, we will assume that the energy gap in the electronic spectrum of HTSCs is 'frozen' [58–61]. This means that it cannot be rapidly destroyed even when the electron temperature T_e considerably differs from the lattice temperature T_p and a sample is found in a metastable state after excitation [58]. It will be shown below that, as a result, the electronic states of a HTSC become degenerate at high excitation levels, i.e. the Fermi levels $E_{e,h}^F$ for free 'electrons' (quasiparticle states above the energy gap in the electronic spectrum) and 'holes' (similar states below the energy gap) do not coincide [59–61]. Taking into account the energy distribution of the electronic state density in the HTSC, this drastically reduces the recombination rate of free electrons and holes, thereby changing the relaxation kinetics of excitation. Second, we will assume that the electronic part of the nonlinear response of HTSCs in nonlinear spectroscopy is caused by interband electronic transitions. Note that the latter assumption is less unexpected than the first one because the role of interband transitions in the formation of the nonlinear response of metals in HTSCs was earlier discussed in papers [8–11, 36, 47, 62–65].

The material of our paper is presented in the following way. In section 2, the physical motivation of the first of the above assumptions is considered according to the approach developed in [58]. After a brief review of some properties of HTSCs of importance to us, we show, by using the model describing the magnetic-dipole formation of the so-called stripe structures (and the energy gap in the electronic spectrum), that the kinetics of a phase transition resulting in the destruction of these structures depends on the initial temperature jump. If an optimally doped HTSC (see below) is not strongly overheated, despite almost instant disappearance of superconductivity, the phase transition should occur comparatively slowly (for 10^{-9} s and slower).

In section 3, we consider a closed system of equations [59] describing the evolution of thermodynamic parameters $E_{e,h}^F$, $T_{e,h}$, and T_p of the electron, hole, and phonon subsystems during and after fast excitation of the HTSC sample by a short pump pulse. It is at this stage that we used the first of the two above assumptions. Here we also present the results of the numerical solution of the system of kinetic equations [59, 61]. It is shown that in the case of a high excitation level in the vicinity of the point $T_0 \simeq T_c$, the kinetics of $E_{e,h}^F$ $T_{e,h}$, and T_p substantially changes due to the appearance of the energy gap in the electronic spectrum of the HTSC.

In section 4, a model of the nonlinear susceptibility of HTSCs is developed which describes the nonlinear responses of a HTSC sample for different modifications of the pump–probe method, including regimes of intense femtosecond and picosecond excitation and one- and two-photon excited-state probing. The model is based on the consistent consideration of contributions from all interband electronic transitions in the 'real' (see below) electronic spectrum [9–11, 64, 66, 67], which considerably reduces the number of fitting parameters in the model.

In section 5, we present the results of numerical simulations of the spectral, temporal, and temperature features of the nonlinear response of the HTSC obtained in all the above-mentioned modifications of the pump–probe method [59–61]. It is at this stage that we use the results of calculation of the kinetics of thermodynamic parameters $E_{e,h}^F$ $T_{e,h}$, and T_p presented in section 3. Note that some of the results presented in this section are original. Finally, we summarise in section 6 the results of our analysis.

2. Self-organisation of charge carriers in HTSCs and phase transition kinetics

2.1 Stripe structures and energy pseudogap

The analysis of investigations of copper–oxide HTSC compounds showed that their metallic conduction is related to the violation of the stoichiometric composition [with a certain defect ('doping') level] [67–70], while the electronic structure is determined by a complicated interaction of well and weakly localised states sensitive to the short-range order. In this case, a rather strong anisotropy leads to the quasi-two-dimensional type of the Fermi surface. The known common property of copper–oxide HTSCs is the ordering of spins of Cu ions in the so-called cuprate (CuO_2) planes. In the case of the stoichiometric composition, these ions (Cu2) have 'holes' with the spin 1/2 in the 3d shell, while the indirect exchange interaction through oxygen ions establishes the long-range antiferromagnetic order at relatively low Neel temperatures $T_N = 300 - 500$ K [71].

The magnetic structure and spin correlations in the metal phase of La_2CuO_4 and $YBa_2Cu_3O_{7-\delta}$ single crystals were investigated in detail by the method of neutron scattering [72]. It was found that the magnetic moments of Cu2 ions in $CuO_2 - Y - CuO_2$ bilayers had the antiferromagnetic ordering, while Cu1 ions in linear $Cu - O$ chains had no magnetic moment. The dependence of the magnetic correlation length ξ_m in the cuprate plane on the average concentration of holes $\langle n \rangle$ was determined by the method of diffuse neutron scattering [73]. The constants of exchange interaction were measured in experiments on inelastic neutron scattering for Cu2 ions ($2J \simeq 0.170$ eV) in bilayers ($2J_b \simeq 10^{-2} 2J$) and $Cu2 - O1$ chains ($2J' \simeq 10^{-5} 2J$), which proved the quasi-two-dimensionality of the spin dynamics in $YBa_2Cu_3O_{7-\delta}$ [74]. Similar results were obtained for $La_{2-\delta}Sr_\delta CuO_4$ [75].

It was shown that, while the energy ('superconducting') gap in LTSCs has the s symmetry and is formed at the temperature lower than T_c due to electron–phonon interaction [75], the experimental data suggest that this gap in HTSCs has either the d symmetry (optimal doping, $\delta = \delta_{opt}$ for which T_c is maximal) or the 'mixed' (s–d) symmetry [76, 77]. Moreover, the so-called pseudogap was found in a $Ba_2Sr_2CaCu_2O_{9-\delta}$ HTSC by the method of angle-resolved photoemission spectroscopy [78] and it was shown that for $\delta = \delta_{opt}$ and $\delta > \delta_{opt}$ (overdoped compounds) the energy gap disappeared at $T = T_c$ at all points on the Fermi surface. For $\delta < \delta_{opt}$ (underdoped compounds), the superconducting gap transforms to the pseudogap upon heating, which has the d symmetry and disappears at $T = T^* \geqslant T_c$. The gap disappears at the point ($\pi/4$, $\pi/4$) of the Brillouin zone at $T = T_c$, while at the point (π, 0) it disappears at $T \simeq 180$ K $\gg T_c$. The nature of the pseudogap and is relation to the superconducting gap are still the object of intense discussions. Although the most convincing experiments were performed only with $Ba_2Sr_2CaCu_2O_{9-\delta}$ (by the method of photoemission spectroscopy), it is assumed that such a behaviour of the energy gap is inherent in all HTSC compounds. Note that two energy gaps with different kinetics were observed in overdoped $YBa_2Cu_3O_{7-\delta}$ with $\delta > \delta_{opt}$ for $T < T_c$ by the method of transient nonlinear spectroscopy [79]. One of them was interpreted as the superconducting gap, while the second one as the pseudogap.

No less interesting data were obtained for La compounds by the methods of electron, neutron, and X-ray scattering [80–82]. It was found that a periodic sequence of alternating strongly elongated regions was formed in cuprate planes at $T = T^*$. These alternating regions, the so-called stripes, were either enriched with holes or almost did not contain them. The correlation length of stripes oriented along the directions (± 1, ± 1, 0) decreases with increasing $\langle n \rangle$. Similar experiments with compounds of Bi, Ba, and Hg did not reveal such properties. At the same time, indirect data on the presence of stripe structures in Bi compounds follow from the measurements of temperature dependences of the heat conductivity and conduction which exhibit breaks [80]. In the opinion of some authors, this demonstrates the dynamic nature of the corresponding stripe structures and their small correlation length.

Stripe structures are described, as a rule, by two methods. The so-called $t - J$ model uses the Hamiltonian describing the kinetic energy and correlations at the neighbouring sites [83]. The model contains two main parameters: the energy t of a hole hopping to neighbouring sites and the exchange interaction energy J with the sites. Sometimes, terms describing hoppings of the holes to more remote sites are also taken into account. Within the framework of the $t - J$ model, the energy band drastically decreases and the effective mass correspondingly increases due to antiferromagnetic spin correlations suppressing hoppings of the holes between neighbouring sites. For $J \gg t$, the separating of phases into layers proves to be energetically profitable, i.e. the formation of alternating regions either filled with holes or virtually devoid of them. The numerical calculations of small two-dimensional clusters of size $\sim 8 \times 8$ show that the phase stratification should be observed for small $\langle n \rangle$ for $J/t \geqslant 1$ [84, 85], whereas $J/t \simeq 0.35$ for real compounds [86].

Another approach – the Peierls–Hubbard model, is based on the consideration of Jahn–Teller distortions of a lattice [87]. Calculations within the framework of this model taking into account hopping of holes between copper sites, single-site Coulomb correlations, the spin dynamics, and kinetic and potential energies of a lattice also confirm the possibility of phase stratification. In this case, distortions of the lattice play a stabilising role and the condition $J/t \geqslant 1$ becomes weaker. However, the simulation is performed for clusters of even a smaller size ($\sim 4 \times 4$), which drastically reduces the accuracy of calculations [88], preventing the description of the kinetics of transitions associated with the formation and destruction of stripe structures.

In the phenomenological model considered below, we will take into account the nonlocal part of the interaction potential of the spin–wave theory [89–91], which has the dipole nature and is caused by deformations of the antiferromagnetic environment, which result in attraction in spin–symmetrical and repulsion in spin–asymmetrical channels [89, 90]. For $J/t \gg 1$, the interaction energy is $\sim 8t^2/J$ [90], whereas for $J/t \ll 1$, the calculation gives the value $\sim J$ [89]. It is this case that we will consider below.

2.2 Magnetic-dipole interaction

Let us assume that the local antiferromagnetic ordering exists in the lattice of HTSC compounds up to the maximum values of δ (for superconductivity) [72]. Assuming that the Coulomb interaction is screened, we consider the magnetic-dipole interaction of holes appearing due to the deformation of the environment, which can be described in the two-particle approximation for the potential energy [89, 90]:

$$V(\boldsymbol{r}, \alpha_1, \alpha_2) = \frac{B \cos(2\theta - \alpha_1 - \alpha_2)}{r^2}. \qquad (2)$$

Here, $\boldsymbol{r}$ is the radius vector connecting two holes; B is a constant related to the modulus $|\boldsymbol{d}_{1,2}^{(m)}| = d^{(m)}$ of their effective dipole moments; and θ and $\alpha_{1,2}$ are the angles between the directions of $\boldsymbol{r}$ and $\boldsymbol{d}_{1,2}^{(m)}$ and the Y axis, respectively. We assume below that $d^{(m)} \equiv 1$. For such a normalisation, in the limiting case $J/t \ll 1$ the constant B/a^2 should be of the order of the exchange interaction energy for a equal to the average distance between holes [89].

Taking the symmetry of the problem into account, we direct the Y axis along one of the possible crystallographic directions – the stripe axis. Let us assume that the dipole moment $\boldsymbol{d}^{(m)}$ of all the holes is oriented parallel to the Y axis

and consider the displacement of one of the holes along the X axis orthogonal to the Y axis (Fig. 3a). By projecting to the X axis the forces acting on this hole from nearest neighbours, we find its potential energy

$$V(x,a) = \frac{B}{a^2}\frac{1-(x/a)^2}{\left[1+(x/a)^2\right]^2}, \tag{3}$$

where x and a are the projections of the radius vector $\boldsymbol{r}$ on the X and Y axes, respectively. By assuming that the dipole moment $\boldsymbol{d}^{(\mathrm{m})}$ can be oriented either along the Y axis or in the opposite direction and $d^{(\mathrm{m})}(y) = d^{(\mathrm{m})}(-y)$, we represent it in the form $d^{(\mathrm{m})}(y) = \pm 1$ and write the expression for the total energy V_{t} of the hole (i.e. the energy taking into account the forces acting on the hole from remote neighbours as well) as

$$V_{\mathrm{t}}(x,a) = \sum_{j=1}^{\infty} d^{(\mathrm{m})}(0)d^{(\mathrm{m})}(ja)V(x,ja). \tag{4}$$

Here, the argument $d^{(\mathrm{m})}$ (i.e. j) numbers in fact the holes in a stripe.

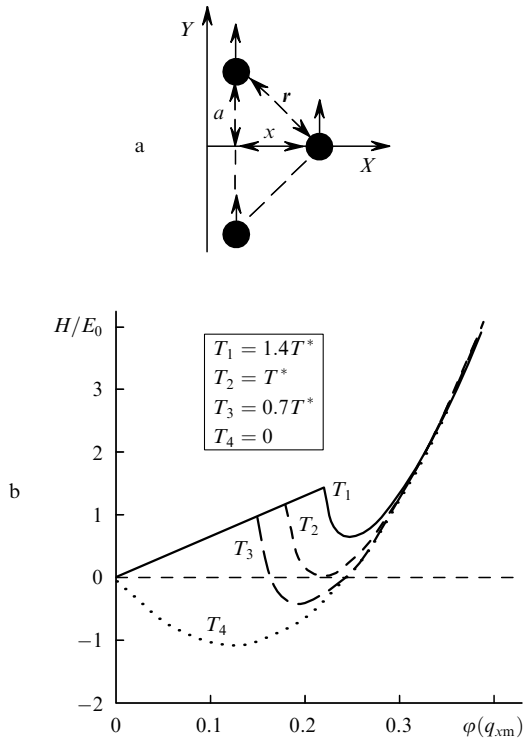

Figure 3. Scheme illustrating the calculation of the interaction energy $V(x,a)$ of a hole with its nearest neighbours (a) and dependences on the normalised localisation energy H of holes on $\varphi(q_{\mathrm{sm}})$ for T_{1-4}; $L = 3$, $G_0 = 4.5$ (b).

When the number of holes with the 'wrong' orientation of $\boldsymbol{d}^{(\mathrm{m})}$ caused by thermal fluctuations in a stripe is small, the standard mean field approximation can be used. To do this, we introduce the mean local (over y) moment $\langle d^{(\mathrm{m})}\rangle(y)$ and will assume that $\langle d^{(\mathrm{m})}\rangle$ is a slow function of y (at the scale of a). Assuming now that the value of $V(x,a)$ decreases with distance considerably faster than $\langle d^{(\mathrm{m})}\rangle$ changes and also assuming that $d^{(\mathrm{m})}(y) - \langle d^{(\mathrm{m})}\rangle(y) \ll \langle d^{(\mathrm{m})}\rangle(y)$, we obtain after replacing summation over j by integration over y and the expansion of $\langle d^{(\mathrm{m})}\rangle(y)$ in a series in the vicinity of arbitrary y that

$$V_{\mathrm{t}}(x,y) \simeq \frac{\pi^2}{6}\frac{B}{a_0^2}d^{(\mathrm{m})}(y)$$

$$\times\left[\langle d^{(\mathrm{m})}\rangle(y) + a_{\mathrm{e}}^2\frac{\mathrm{d}^2\langle d^{(\mathrm{m})}\rangle(y)}{\mathrm{d}y^2} + \ldots\right]\left[1+\left(\frac{x}{a_0}\right)^2\right]^{-1}. \tag{5}$$

Here, $a_0 = (6/\pi^2)a$; a_{e} is a constant of the order of the magnetic correlation length related to the finite value of the interaction radius. It follows from (5) that interaction inside a stripe is well localised.

We will assume below that the distribution of stripes along the X axis is periodic and consider the period L of this distribution and the spatial frequency $q_{x\mathrm{m}} = 2\pi/L$ of its lowest harmonic as the external parameters of the problem rigidly connected with δ (i.e. with $\langle n\rangle$). To calculate the spatial distribution of the potential energy $V_0(x,y)$ for an arbitrary distribution of stripes along the X axis, we will find the Fourier transform of the function $V_{\mathrm{t}}(x,y)$ (5)

$$V_{\mathrm{t}}(q_x,y) = L^{-1}\int_{-L/2}^{L/2} V_{\mathrm{t}}(x,y)\exp(\mathrm{i}q_x x)\mathrm{d}x$$

$$\approx \tilde{G}(y)\exp(-q_x a_0), \tag{6}$$

where

$$\tilde{G}(y) = G_0 d^{(\mathrm{m})}(y)\left[\langle d^{(\mathrm{m})}\rangle(y) + a_{\mathrm{e}}^2\frac{\mathrm{d}^2\langle d^{(\mathrm{m})}\rangle(y)}{\mathrm{d}y^2} + \ldots\right];$$

$$G_0 = \frac{3}{\pi}\frac{B}{a_0 L};$$

and q_x is the spatial frequency. For small values of δ, taking into account screening at distances of the order of a few periods of a cell, the integration limits in (6) can be expanded to infinity.

For an arbitrary one-dimensional (along x) distribution of stripes with the same $\langle d^{(\mathrm{m})}\rangle(y)$ and $n(q_x)$, the energy distribution density is

$$V_0(q_x,y) = V_{\mathrm{t}}(q_x,y)n(q_x) = \tilde{G}(y)\exp(-q_x a_0)n(q_x). \tag{7}$$

After the inverse Fourier transform of (7) and the renormalisation

$$\tilde{G} \to \frac{\tilde{G}}{E_0}, \quad x \to \frac{x}{a}, \quad L \to \frac{L}{a}, \quad a_{0,\mathrm{e}} \to \frac{a_{0,\mathrm{e}}}{a},$$

where $E_0 = (2\pi\hbar)^2/(2m_0a^2)$, $\hbar$ is Planck's constant, and m_0 is the effective mass, the stationary Schrödinger equation can be written in the form

$$\left[\frac{\mathrm{d}^2}{\mathrm{d}x^2} + \tilde{G}(y)\exp\left(-\mathrm{i}a_0\frac{\mathrm{d}}{\mathrm{d}x}\right)|\varphi(x,y)|^2 + \varepsilon_H\right]\varphi(x,y) = 0. \tag{8}$$

Here, $\varphi(x,y)$ is the wave function of a hole and ε_H is the eigenvalue of the energy operator. The differential operator in the exponent in (8) takes into account the nonlocal interaction and acts on $|\varphi(x,y)|^2$. For two stripe systems (with subscripts 1 and 2), for which $\langle d_1^{(\mathrm{m})}\rangle(y) = -\langle d_2^{(\mathrm{m})}\rangle(y)$, expression (8) transforms to the system

$$\left\{\frac{\mathrm{d}^2}{\mathrm{d}x^2}+\tilde{G}(y)\exp\left(-\mathrm{i}a_0\frac{\mathrm{d}}{\mathrm{d}x}\right)\left[|\varphi_k(x,y)|^2 - |\varphi_l(x,y)|^2\right]+\varepsilon_H\right\}\varphi_k(x,y)=0, \tag{9}$$

where k, $l=1$, 2 and $k\neq 1$.

Note that for the solutions of (9) of interest to us, the values of ε_H and $\langle d_{1,2}^{(\mathrm{m})}\rangle(y)$ entering into the expression for $\tilde{G}(y)$ should be consistent with the wave function $\varphi_{1,2}(x,y)$. In this case, by averaging $d^{(\mathrm{m})}$ in each stripe over two admissible directions taking into account thermal fluctuations in the local (over y) thermodynamic equilibrium, we should require [92] that

$$\langle d_{1,2}^{(\mathrm{m})}\rangle(y)=\pm\tanh\left[\frac{\Delta_{\mathrm{d}}(y)}{k_{\mathrm{B}}T}\right]. \tag{10}$$

Here, $2\Delta_{\mathrm{d}}(y)$ is the difference in the interaction energies for holes with the dipole moment $\boldsymbol{d}^{(\mathrm{m})}$ oriented along the vector $\langle\boldsymbol{d}^{(\mathrm{m})}\rangle(y)$ in a stripe (the order parameter) and in the opposite direction. Simultaneously, the relation

$$\Delta_{\mathrm{d}}(y)=-\sum_{p=-\infty}^{\infty}\sum_{i,j=1,2}(-1)^{i-j}\tilde{G}(y) \times\exp(-|p|q_{x\mathrm{m}}a_0)n_i(pq_{x\mathrm{m}},y)n_j(-pq_{x\mathrm{m}},y) \tag{11}$$

should be fulfilled.

The normalisation of $\varphi_{1,2}(x,y)$ in calculations corresponded to the arrangement of two holes with the opposite orientations of $\boldsymbol{d}^{(\mathrm{m})}$ over the period L (in the 'unit cell') of the stripe structure [93]:

$$\int_{-L/2}^{L/2}\int_{-L/2}^{L/2}\mathrm{d}x\mathrm{d}y|\varphi_k(x,y)|^2=1, \tag{12}$$

where $k=1$, 2. Thus, the probability of finding any hole in any stripe was the same.

We described the dynamics by assuming that $\langle d^{(\mathrm{m})}\rangle$ depends explicitly not only on y but also on the time t and the so-called relaxation approximation [93] is used

$$\frac{\partial\langle d^{(\mathrm{m})}\rangle(y,t)}{\partial t}=-\tau_{\mathrm{d}}^{-1}\left[\langle d^{(\mathrm{m})}\rangle(y,t)-\langle d^{(\mathrm{m})}\rangle_0\right]. \tag{13}$$

Here, τ_{d} is the flip time of $d^{(\mathrm{m})}$ and $\langle d^{(\mathrm{m})}\rangle_0$ is the equilibrium value of $\langle d^{(\mathrm{m})}\rangle$. Dynamic terms were not explicitly included into system (9), and the evolution of $\varphi_{1,2}(t)$ was described in terms of the dependence $\langle d^{(\mathrm{m})}\rangle(y,t)$ in the adiabatic approximation (the time scale was specified by the parameter $\tau_{\mathrm{F}}=L/v_{\mathrm{F}}$, where v_{F} is the Fermi velocity) by using Eqn (13).

2.3 Stationary stripe structures

Taking (9) into account, we write the Hamiltonian of the system in the form

$$H=\sum_{q_x;\,i\neq j=1,2}q_x^2\varphi_i(q_x,y)\varphi_i(-q_xy)-\tilde{G}(y)\exp(-q_xa_0) \times n_i(q_x,y)n_i(-q_x,y)+\tilde{G}(y)\exp(-q_xa_0)n_i(q_x,y)n_j(-q_x,y). \tag{14}$$

Then, it follows from the Cauchy–Schwartz inequality [94] that the minimisation of H occurs for

$$\varphi_i(q_x,y)=-\varphi_j(q_x,y),\ \text{if}\ q_x=\pm q_{x\mathrm{m}},\pm 3q_{x\mathrm{m}},\ \ldots,$$
$$\varphi_i(q_x,y)=\varphi_j(q_x,y),\ \text{if}\ q_x=0,\pm 2q_{x\mathrm{m}},\ldots, \tag{15}$$

which is equivalent to the requirement

$$\varphi_1(x,y)=\varphi_2\left(x\pm\frac{L}{2},y\right). \tag{16}$$

Because in the case of the coexistence of stripe structures, at least one spatial harmonic should have the amplitude $\varphi_{1,2}(q_{x\mathrm{m}})\neq 0$, taking the two lowest harmonics $\varphi_{1,2}$ into account, we write

$$\varphi_{1,2}(x,y)=\varphi_0(y)\pm\varphi(q_{x\mathrm{m}},y)\cos(q_{x\mathrm{m}}x). \tag{17}$$

In this case, the expressions for the localisation energy of holes H and Δ_{d} will take the form

$$H(y)=2\varphi^2(q_{x\mathrm{m}},y)L^{-1}\left\{\pi^2-8L^2\varphi_0^2(y) \times\left[\langle d^{(\mathrm{m})}\rangle(y)+a_{\mathrm{e}}^2\frac{\mathrm{d}^2\langle d^{(\mathrm{m})}\rangle(y)}{\mathrm{d}y^2}+\ldots\right]G_0\exp(-q_{x\mathrm{m}}a_0)\right\}, \tag{18}$$

$$\Delta_{\mathrm{d}}(y)=8L^2\varphi_0^2(y)\varphi^2(q_{x\mathrm{m}},y) \times\left[\langle d^{(\mathrm{m})}\rangle(y)+a_{\mathrm{e}}^2\frac{\mathrm{d}^2\langle d^{(\mathrm{m})}\rangle(y)}{\mathrm{d}y^2}+\ldots\right]G_0\exp(-q_{x\mathrm{m}}a_0). \tag{19}$$

By using relations (10), (12), (18), and (19), we can calculate the dependence of H (i.e. the pseudogap width) on $\varphi(q_{x\mathrm{m}})$ in the thermodynamic equilibrium state, when $\varphi_0(y)=\varphi_0$ and $\varphi(q_{x\mathrm{m}},y)=\varphi(q_{x\mathrm{m}})$ (Fig. 3b). One can see that in this case there exists the region of parameters where the minimisation of H for $T<T^*=\mathrm{const}$ occurs for $\varphi(q_{x\mathrm{m}})\neq 0$. The critical temperature T^* determines the point of phase transition related to the formation of stripe structures. However, even more important for us is that the dependence of $\varphi(q_{x\mathrm{m}})$ on H is ambiguous and stripe structures may not be destructed upon 'rapid' excitation but transfer to metastable states.

More rigorous calculations were performed numerically taking into account the six first harmonics of the Fourier expansion of $\varphi_{1,2}(x)$ [58]. In this case, the auxiliary Hamiltonian

$$H'=\sum_{p=-\infty}^{\infty}\sum_{i,j=1,2}\left[(pq_{x\mathrm{m}})^2\varphi_i(pq_{x\mathrm{m}})\varphi_i(-pq_{x\mathrm{m}}) -\langle d^{(\mathrm{m})}\rangle_i(-1)^{i-j}G_0\exp(-|p|q_{x\mathrm{m}}a_0)n_i(pq_{x\mathrm{m}})n_j(-pq_{x\mathrm{m}})\right] +M\exp\left\{R[Ln_i(0)-1]^2\right\},$$
$$\langle d^{(\mathrm{m})}\rangle_i=\tanh\left[(k_{\mathrm{B}}T)^{-1}\langle d^{(\mathrm{m})}\rangle_i \times\sum_{p=-\infty}^{\infty}\sum_{i,j=1,2}(-1)^{i-j}G_0\exp(-|p|q_{x\mathrm{m}}a_0)n_i(pq_{x\mathrm{m}})n_j(-pq_{x\mathrm{m}})\right] \tag{20}$$

was constructed, which was minimised by the unlimited simplex method [95] to provide the correct normalisation of $\varphi_{1,2}(x)$ for $R \to \infty$. The parameters M and R were selected to provide the normalisation error less than 1 %. The binding energy was determined by substituting the found functions $\varphi_{1,2}(x)$ into (14). The normalised calculated dependence $T^*(L^{-2})$ is illustrated in Fig. 4a. One can see that the region of existence of stripe structures is restricted by the limiting value $\delta_{\max}$ for which $T^* = 0$. The dependence $T^*(L^{-2})$ has the region of an almost linear increase in T^* with decreasing L (i.e. δ). The functions $\varphi_{1,2}(x)$ are strongly anharmonic (Fig. 4b). The energy gap decreases monotonically with increasing T and vanishes at $T = T^*$ (Fig. 4c). This confirms indirectly that the point $T = T^*$ is the point of the second-order phase transition.

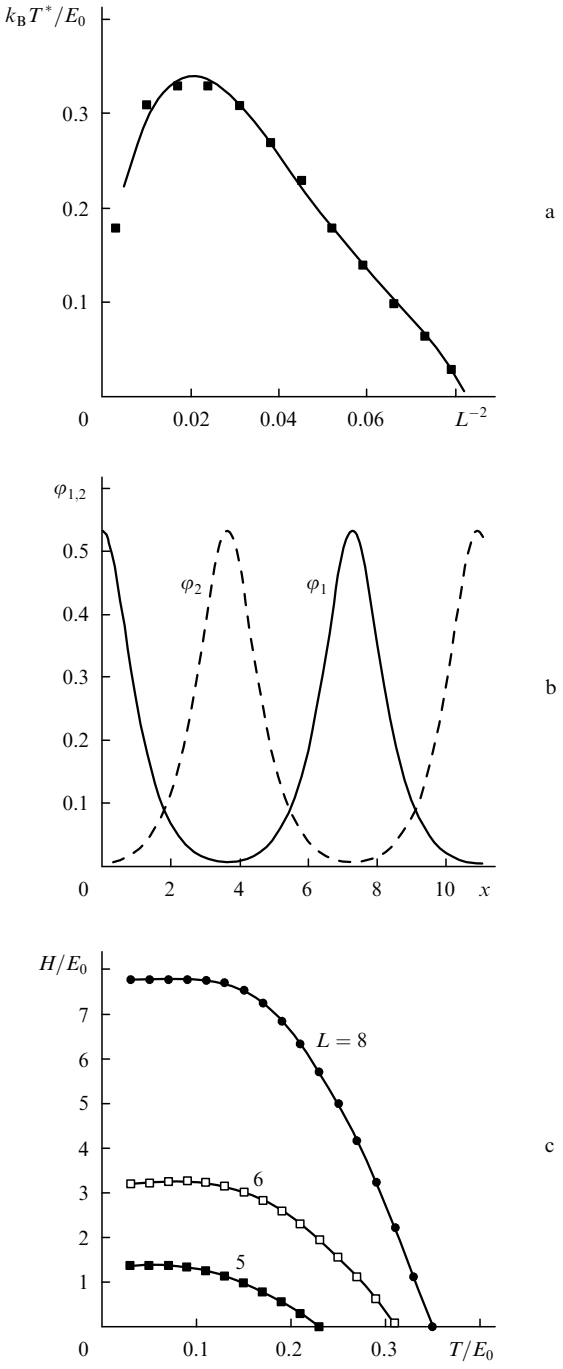

Figure 4. Normalised dependence of T^* on L^{-2} (squares) and its approximation by the fourth-order polynomial (solid curve) (a), wave functions $\varphi_{1,2}(x)$ (solid and dashed curves) for $L = 7.5$ (b), and the temperature dependence of the pseudogap width for $L = 5$, 6, and 8; $G_0 = 4.5$ (c).

2.4 Phase coexistence

By assuming that $\langle d^{(m)}\rangle(y) \neq \text{const}$ and taking into account the term proportional to $d^2\langle d^{(m)}\rangle(y)/dy^2$, we perform the variation of $\varphi(q_x, y)$ (17) with changing continuously the position of a local extremum. It can be easily shown that the minimisation of H occurs for

$$\varphi(q_{xm}, y) = (2L)^{-1}\left(1 - \frac{\gamma}{P}\right), \tag{21}$$

where

$$\gamma = (4g)^{-1} = \frac{\pi^2}{4LG_0 \exp(-q_{xm}a_0)};$$

$$P = \langle d^{(m)}\rangle(y) + a_e^2 \frac{d^2\langle d^{(m)}\rangle(y)}{dy^2} + \ldots.$$

In this case,

$$\Delta_d(y, P) = \frac{G_0 P}{L}\left[1 - \left(\frac{\gamma}{P}\right)^2\right]\exp(-q_{xm}a_0). \tag{22}$$

By substituting now (22) into (10) and linearising the obtained equation for P, taking into account the self-consistence of the problem, we obtain the closed equation

$$a_e^2 \frac{d^2\langle d^{(m)}\rangle(y)}{dy^2} = E_b(T)\text{arctanh}\left[\langle d^{(m)}\rangle(y)\right] + \gamma - \langle d^{(m)}\rangle(y), \tag{23}$$

where

$$E_b(T) = \frac{k_B TL}{2G_0 \exp(-q_{xm}a_0)},$$

which can be interpreted within the framework of a mechanical analogy as the equation of motion in the potential

$$U\left(\langle d^{(m)}\rangle\right) = -E_b(T)\left\{\text{arctanh}\left[\langle d^{(m)}\rangle(y)\right] + \frac{1}{2}\ln\left(1 - \langle d^{(m)}\rangle^2\right)\right\} - \gamma\langle d^{(m)}\rangle + \frac{1}{2}\langle d^{(m)}\rangle^2. \tag{24}$$

Its nature is illustrated in Fig. 5a. For $T = T^*$, both maxima of the potential curve $U(\langle d^{(m)}\rangle)$ have the same value. Note that the system is conservative in the case under study, and all processes proceed in it with the conservation of energy.

Consider now the simplest example of the inhomogeneous (over y) solution of the phase switching type. We will assume that $\langle d^{(m)}\rangle(y)|_{y\to-\infty} = \langle d^{(m)}\rangle_1$ and $\langle d^{(m)}\rangle(y)|_{y\to+\infty} = \langle d^{(m)}\rangle_2 \neq \langle d^{(m)}\rangle_1$ on two infinitely remote (over y) sides of the cuprate plane. We are interested in the interface between these regions, which we will call phases. It follows from Fig. 5a that for $T < T_m = \text{const} > T^*$, the curves

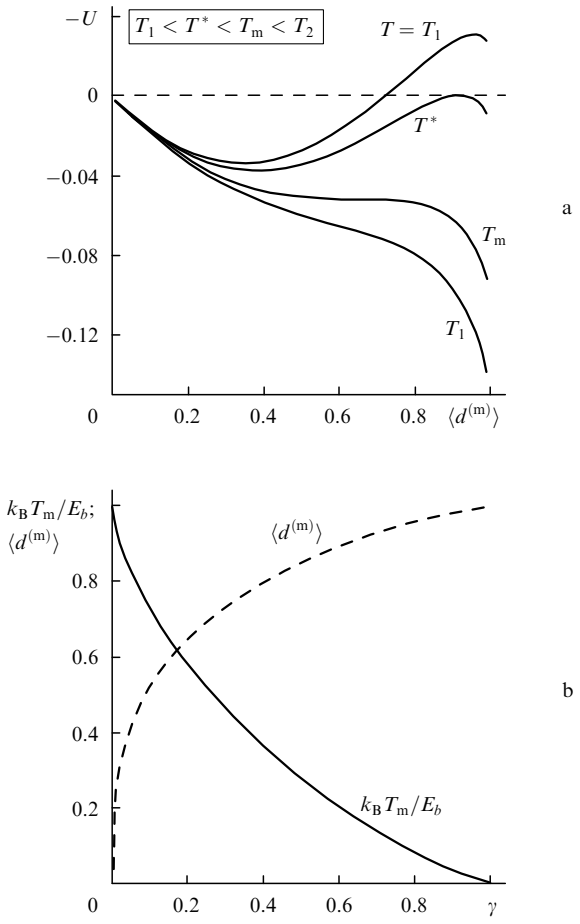

Figure 5. Dependences $U(\langle d^{(m)} \rangle)$ calculated for different T (a) and normalised dependences $T_m(\gamma)$ (solid curve) and $\langle d^{(m)} \rangle_r(\gamma)$ (dashed curve) calculated for $T = T_m$ (b).

$U[\langle d^{(m)} \rangle(y)]$ have two local extrema. The first of them, U_1, is localised at the point $\langle d^{(m)} \rangle = 0$ at any T, while the position $\langle d^{(m)} \rangle = \langle d^{(m)} \rangle_r$ of the second extremum U_2 depends on T. For $T^* < T < T_m$, we have $U_1 < U_2$, and for $T < T^*$, we have $U_1 > U_2$. For $T = T^*$, the phases have the same energy, $U_1 = U_2$, and solutions can be obtained with the asymptotic transition

$$\left. \frac{\mathrm{d}\langle d^{(m)} \rangle(y)}{\mathrm{d}y} \right|_{y \to \pm\infty} = 0 \tag{25}$$

from the phase $\langle d^{(m)} \rangle_1 = 0$ to the phase $\langle d^{(m)} \rangle_2 = \langle d^{(m)} \rangle_r$ in accordance with the Maxwell rule [96].

The approximate estimate of the width of the phase transition region can be obtained analytically because the solution of (23) under condition (25) can be written in quadratures:

$$\zeta - \zeta_0 = \int_0^{\langle d^{(m)} \rangle_r} \mathrm{d}\langle d^{(m)} \rangle \left\{ E_b(T^*) \left[\operatorname{arctanh}\langle d^{(m)} \rangle + \right.\right.$$

$$\left.\left. + \frac{1}{2} \ln\left(1 - \langle d^{(m)} \rangle^2\right) \right] + \gamma \langle d^{(m)} \rangle - \frac{1}{2} \langle d^{(m)} \rangle^2 \right\}^{-1/2}, \tag{26}$$

where $\zeta = y/a_e$ and $\zeta_0 = \text{const}$. By expanding the integrand into a series and retaining quadratic terms for $E_b(T^*) \ll 1$, we obtain

$$\langle d^{(m)} \rangle(\zeta) = \frac{1}{2} \frac{E_b(T^*) + \gamma}{1 - E_b(T^*)}$$

$$\times \left\{ \sin\left\{ \left[\frac{1}{2} \left[1 - E_b(T^*)\right] \right]^{1/2} (\zeta - \zeta_0) \right\} + 1 \right\}. \tag{27}$$

This gives the estimate of the width of the phase transition region:

$$\Delta y = \pi a_e \left[\frac{2}{1 - E_b(T^*)} \right]^{1/2}. \tag{28}$$

It is obvious that this solution is invariant with respect to an arbitrary displacement $y \to y + \delta y$ ($\delta y = \text{const}$) of coordinates along the Y axis.

2.5 Metastable states and phase transition kinetics

The second maximum in the potential curve in Fig. 5a disappears at the temperature $T = T_m$ corresponding to the simultaneous fulfilment of the conditions

$$\frac{\partial}{\partial \langle d^{(m)} \rangle} U\left(\langle d^{(m)} \rangle, T_m\right) = 0,$$

$$\frac{\partial^2}{\partial \langle d^{(m)} \rangle^2} U\left(\langle d^{(m)} \rangle, T_m\right) = 0. \tag{29}$$

Figure 5b illustrates the normalised dependence $T_m(\gamma)$. It is easy to verify that $T_m > T^*$. Consider now the situation when $T^* \neq T < T_m$ and the phase interface is movable. We assume, as before, that $\langle d^{(m)} \rangle(y)|_{y \to -\infty} = 0$ and $\langle d^{(m)} \rangle(y)|_{y \to +\infty} = \langle d^{(m)} \rangle_r$, and will describe the interface by the profile of the phase switching wave $\langle d^{(m)} \rangle(y, t) = \langle d^{(m)} \rangle(\xi)$ moving along the Y axis at a constant velocity v. Here, $\xi = (y - vt)$ is the running coordinate. By performing similar transformations and using (13), we obtain the relation

$$a_e^2 \frac{\mathrm{d}^2 \langle d^{(m)} \rangle}{\mathrm{d}\xi^2} = E_b(T)$$

$$\times \operatorname{arctanh}\left(\langle d^{(m)} \rangle - \tau_d v \frac{\mathrm{d}\langle d^{(m)} \rangle}{\mathrm{d}\xi} \right) + \gamma - \langle d^{(m)} \rangle, \tag{30}$$

which transforms to (23) for $v = 0$. This means that for $T = T^*$, the phase switching wave is immobile. Because, within the framework of a mechanical analogy, the term proportional to v is responsible for nonlinear friction, the phase coexistence at $T \neq T^*$ is impossible. This conclusion is consistent with the fact that for the switching wave to develop in distributed systems, the initial seed is necessary – a fluctuation with the characteristic size of the order of the transition region width [97, 98]. The velocity v depends on the value of the control parameter (in our case, T). At the critical point, $v = 0$ and changes the sign.

Equation (3) was solved by using the six-order Runge–Kutta method with a time variable step t. We considered the evolution of the initial state $\langle d^{(m)} \rangle = 0$ with the hyper-Gaussian perturbation. Figure 6a illustrates the evolution of a broad (compared to Δy) initial fluctuation for $T > T^*$. The system rapidly undergoes a transition to the metastable state $\langle d^{(m)} \rangle = \langle d^{(m)} \rangle_r$, and only then a switching wave to the phase $\langle d^{(m)} \rangle = 0$ is formed, the value of $\langle d^{(m)} \rangle_r$ being decreased with increasing T. For $T = T^*$ (Fig. 6b) and

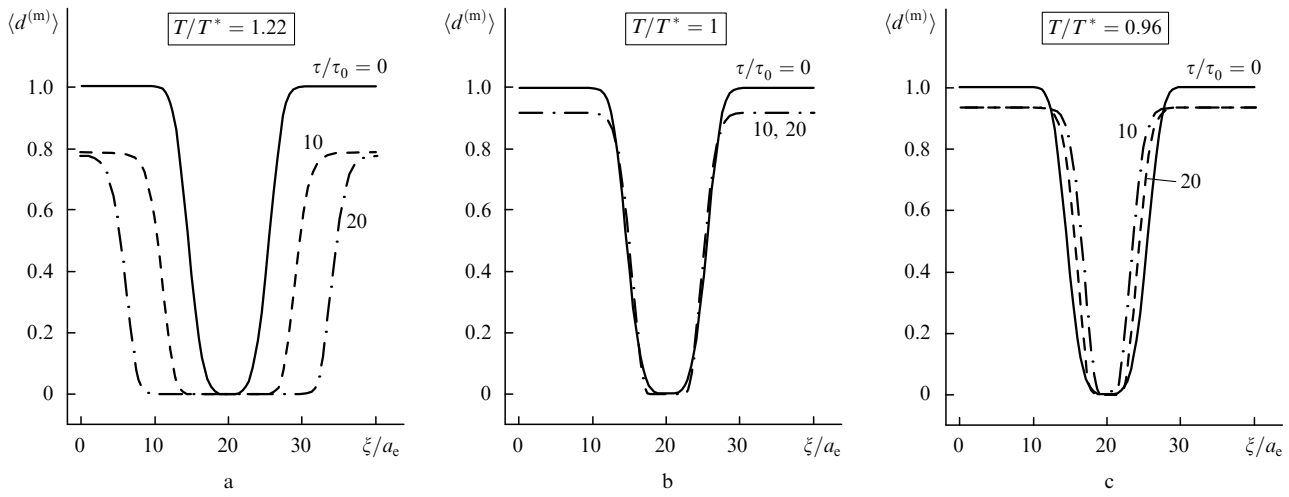

Figure 6. Temporal evolution of the initial fluctuation $\langle d^{(m)} \rangle$ for $T/T^* = 1.22$ (a), 1.00 (b), and 0.96 (c); $g = 1.25$.

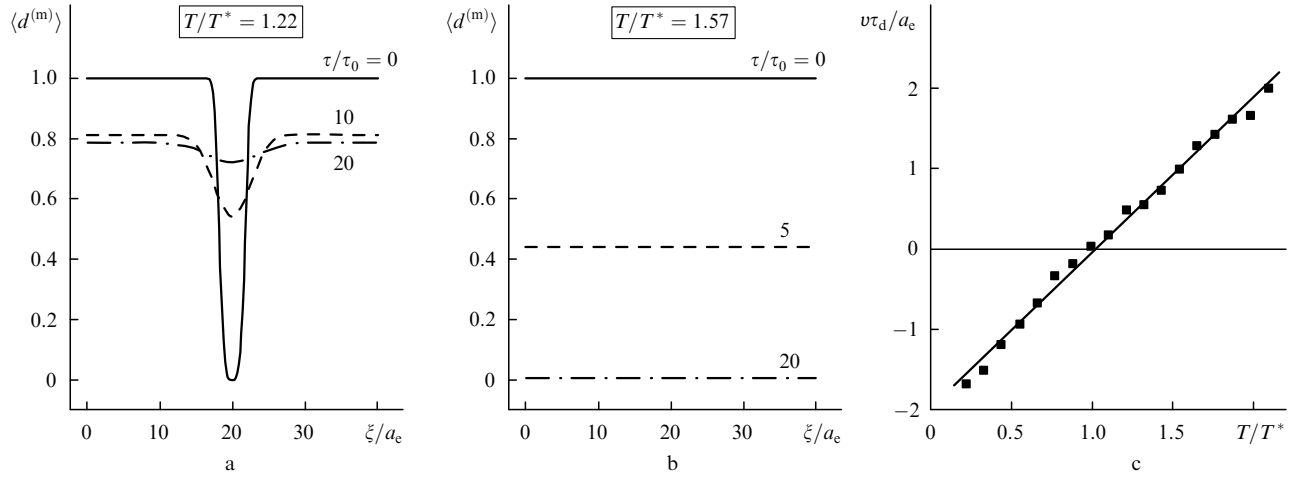

Figure 7. 'Spreading' of the narrow fluctuation $\langle d^{(m)} \rangle$ for $T/T^* = 1.22$ (a), scenario of the phase transition for $T > T_m$ (b), and the normalised dependence of the velocity v on T/T^*; $g = 1.25$.

$T < T^*$ (Fig. 6c), the system first undergoes a transition to the metastable state $\langle d^{(m)} \rangle = \langle d^{(m)} \rangle_r$, and then fluctuations are either 'frozen' ($v = 0$, the stationary phase interface) or 'resolved' ($v < 0$). A narrow fluctuation resolves even for $T > T^*$ (Fig. 7a). For $T > T_m$, the system undergoes a transition from the state $\langle d^{(m)} \rangle \neq 0$ at once to the state $\langle d^{(m)} \rangle = 0$ (Fig. 7b). The velocity v linearly depends on T/T^*, by changing its sign at the point $T = T^*$ (Fig. 7c).

Thus, if the two phases can coexist at $T = T^*$ (Fig. 7b), then for $T < T^*$ ($v > 0$) the seed of the stripe structure can expand due to the involvement of the holes from regions where the order has not been established yet (Fig. 6a). By assuming that the magnetic dipole moments $\boldsymbol{d}^{(m)}$ in a stripe are ordered for $\sim 10^2$ holes and $\tau_d \sim 10^{-12} - 10^{-13}$ s, we obtain the estimate for the propagation time of a phase switching wave $\tau_v \sim 0.1 - 1.0$ ns. However, for such a wave to begin propagate, the size of the stripe seed should exceed Δy (see Figs 6a and 7a). Figure 8a illustrates the calculated dependence of $\Delta y(T/T^*)$ (at the 0.9 level of the front height) for $g = 1.25$ (solid curve) and 0.56 (dashed curve). Therefore, by taking into account the calculated values of Δy, we estimate the minimal size of the seed (in fact, the number of holes with ordered $\boldsymbol{d}^{(m)}$) as $\Delta y \sim 4 - 6$ and obtain the probabilistic estimate of the formation time τ_f corresponding to $\tau_f \sim 10$ ns $\gg \tau_d$ of the initial fluctuation

$$\tau_f = \frac{\tau_d}{\left(1 - \langle d^{(m)} \rangle_r\right)^{N-1}}. \tag{31}$$

It follows from this that for $T/T^* \sim 1.25$, when $(1 - \langle d^{(m)} \rangle_r) \sim 0.25$ (see Fig. 8b), the formation time is $\tau_f \sim 10$ ns $\gg \tau_d$.

Thus, we described in this section the self-organisation of charge carriers in a HTSC due to magnetic-dipole interaction. It was shown that for a reasonable value of the energy $G_0 \sim 100$ meV, the limiting HTSC doping level $\langle n \rangle_{max} \sim 1.125$, the formation temperature of stripe structures $T^* \sim 150$ K, their spatial period, the presence of the linear region of the dependence $T^*(\langle n \rangle)$ for $\langle n \rangle < \langle n \rangle_{max}$, the energy gap width and its temperature dependence correspond to the experimental data. However, it is even more important that, despite a rapid destruction of superconductivity upon impact excitation of initially superconducting HTSCs up to $T > T_c$, metastable stripe structures in their cuprate planes can exist for a long time (~ 1 ns and longer, see above). It is for this reason that a sample can 'remember' its initial state during all this time.

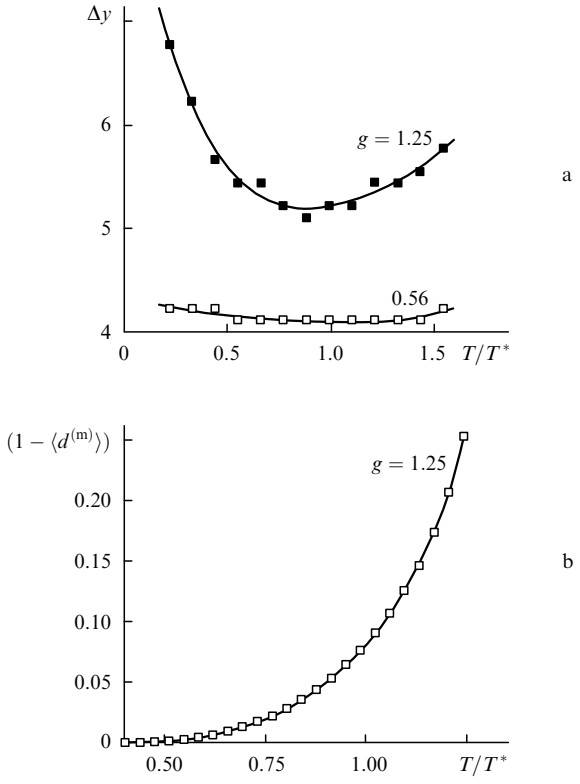

Figure 8. Temperature dependences of the transition region width Δy for $g = 1.25$ and 0.56 (a) and the dependence of $(1 - \langle d \rangle_r)$ on T/T^* for $g = 1.25$ (b).

3. Nonequilibrium HTSC thermodynamics at high excitation levels

3.1 Kinetic equations

Having substantiated the metastable nature of stripe structures existing in HTSCs, we now turn to the construction of a simplified system of kinetic equations describing the evolution of the thermodynamic parameters of the system upon optical excitation.

In the case of a 'frozen' energy gap, the electronic spectrum of a HTSC is similar to that of an intrinsic narrow-gap semiconductor. Therefore, according to [59–61], it is convenient to introduce two bands (similar to the valence and conduction bands in a semiconductor) separated by the energy gap of width Δ, and to consider the evolution of the concentrations $N_{e,h}$ of free 'electrons' (quasi-particle states over the gap) and 'holes' (quasi-particle states below the gap), respectively. If we now assume that intraband thermalisation (intraband e–e relaxation) occurs infinitely rapidly, the energy distributions $E_{e,h}$ of electrons and holes at any instant t can be considered quasi-equilibrium. In this case, the description of the evolution of the system becomes parametrical and is reduced to the introduction of the dependence of the instant values of $E_{e,h}^F$ and $T_{e,h}$ on time t. Therefore, in all further calculations we will substitute the instant values of $E_{e,h}^F$ and $T_{e,h}$ at each instant t to the standard Fermi–Dirac distribution function f_F $(E_{e,h};\ E_{e,h}^F,\ T_{e,h})$. The concentrations $N_{e,h}$ of free electrons and holes and the energy density stored in these two subsystems ('heat' storage) $Q_{e,h}$ are described by the expressions

$$N_{e,h} = N_c \int_0^\infty f_F\left(E_{e,h}; E_{e,h}^F, T_{e,h}\right) g_{e,h}(E_{e,h}; \Delta) \mathrm{d}E_{e,h}, \qquad (32)$$

$$Q_{e,h} = N_e \langle E_{e,h} \rangle$$

$$= N_e \int_0^\infty E_{e,h} f_F\left(E_{e,h}; E_{e,h}^F, T_{e,h}\right) g_{e,h}(E_{e,h}; \Delta) \mathrm{d}E_{e,h}. \qquad (33)$$

Here, N_c is the density of cells; $g_{e,h}(E_{e,h}; \Delta)$ are functions describing the electronic-states densities at a fixed gap width Δ; and $\langle E_{e,h} \rangle$ are the mean energies of free electrons and holes. Taking into account the symmetry of the problem and that photogeneration of free electrons and holes and their recombination are pair processes, we will assume that the states of both subsystems at each instant t are identical and

$$g(E; \Delta) \equiv g_e(E; \Delta) = g_h(E; \Delta), \qquad (34)$$

$$E^F \equiv E_e^F = E_h^F,\ T_e = T_h,\ \langle E_e \rangle = \langle E_h \rangle,\ N_e = N_h,\ Q_e = Q_h.$$

Taking this into account, it is sufficient to write kinetic equations for N_e and Q_e.

The first of them can be written by assuming that photogeneration and recombination of free carriers are strictly pair processes. Then, we obtain

$$\frac{\mathrm{d}N_e}{\mathrm{d}t} = \left[1 - f_F(\langle E_e \rangle; E^F, T_e)\right]$$

$$\times P_p(t) \frac{N_e}{Q_e} \frac{\hbar\omega}{2} - \gamma_{eh}^{(r)} \left(N_e^2 - N_s^2\right). \qquad (35)$$

Here, $P_p(t)$ is the instant density of the flux of absorbed pump photons of energy $\hbar\omega$; $\gamma_{eh}^{(r)} = \gamma_{ehp}^{(r)} + \gamma_{ehe}^{(r)}$ is the rate constant of nonradiative pair recombination represented by a sum of rate constants describing three-particle processes involving a phonon $\gamma_{ehp}^{(r)}$ and one more electron (hole) $\gamma_{ehe}^{(r)}$ and depending on Δ, E^F, $T_{e,p}$, N_e and other parameters [99]; $N_s = N_c \int_0^\infty f_F(E_e; E_0^F, T_p) g(E_e; \Delta) \mathrm{d}E_e$ is the quasi-equilibrium concentration of electrons and holes for $E^F = E_0^F$ and $T_e = T_p \neq T_0$. The term in the right-hand part of (35) describing the generation of free carriers takes into account explicitly that upon absorption of a photon, a hot electron appears in the conduction band, which experiences the instant interband e–e scattering accompanied by the production of $\frac{1}{2}\hbar\omega / \langle E_e \rangle$ thermalised electrons and holes with $\langle E_e \rangle = Q_e / N_e$. Taking into account a competition between interband and intraband e–e scattering, the factor $[1 - f_F(\langle E_e \rangle; E^F, T_e)]$ changes from 1/2 (for $E^F \gg \Delta/2$) to 1 (for $E^F \ll \Delta/2$).

The initial (E') and final ($E'' \simeq E' + 2\langle E_e \rangle$) states of the third quasi-particle involved in pair recombination cannot be completely empty and occupied, respectively. In the case of degeneracy (when $E^F \geqslant \Delta/2$ and the Fermi level 'enters' into the conduction band) due to the presence of a peak in the distribution of the state density $g(E_e)$ in the HTSC in the vicinity of the point $E_e = \Delta/2$, this condition reduces the concentration of quasi-particles that can be involved in recombination. The larger is the gap width Δ, the higher is the degree of degeneracy; and the lower is T_e, the more distinct should be this effect. We took the role of this effect into account within the framework of the expression

$$\gamma_{ehe}^{(r)} \simeq \tilde{\gamma}_{ehe}^{(r)} N_e', \tag{36}$$

where $\tilde{\gamma}_{ehe}^{(r)}$ is the rate constant of recombination, which is independent of the concentration of third quasi-particles, and

$$N_e' \simeq N_c \int_0^\infty dE' f_F(E'; E^F, T_e)\left[1 - f_F(E' + 2\langle E_e\rangle; E^F, T_e)\right]$$

$$\times g(E')g(E' + 2\langle E_e\rangle) \leqslant N_e. \tag{37}$$

If the third particle involved in recombination is an acoustic phonon, the rate constant $\gamma_{ehp}^{(r)}$ of the corresponding process also should decrease with increasing the total energy $2\langle E_e\rangle$ of recombining particles because phonons with the maximal energy E_{max} can no longer take away this energy. In the isotropic approximation for the model dispersion dependence [99]

$$E_{ph} \simeq E_{max} \sin\frac{\pi}{2}\frac{K}{K_{Br}} \tag{38}$$

this results in the appearance of the correcting factor in the recombination constant $\gamma_{ehp}^{(r)}$, which can be taken into account by making the replacement

$$\gamma_{ehp}^{(r)} \to \gamma_{ehp}^{(r)}(\langle E_e\rangle)$$

$$= \tilde{\gamma}_{ehp}^{(r)} \int_0^{E_{max}} dE_{ph} F(E_{ph}; T_p) G(E_{ph}) G(E_{ph} + 2\langle E_e\rangle), \tag{39}$$

where $\tilde{\gamma}_{ehp}^{(r)}$ is a constant independent of T_p and $\langle E_e\rangle$; E_{ph} and K are the phonon energy and momentum; E_{max} is the phonon energy at the edge of the Brillouin zone ($K = K_{Br}$);

$$F(E_{ph}; T_p) = \left[\exp\left(\frac{E_{ph}}{k_B T_p}\right) - 1\right]^{-1} \tag{40}$$

is the distribution function; and

$$G(E_{ph}) = \begin{cases} \left(E_{max}^2 - E_{ph}^2\right)^{-1} \arcsin\left(\dfrac{E_{ph}}{E_{max}}\right) \text{ for } E_{ph} \leqslant E_{max}, \\ 0 \text{ for } E_{ph} > E_{max} \end{cases} \tag{41}$$

is the phonon state density.

The kinetic equation for Q_e can be obtained by representing Q_e in the form

$$Q_e = Q_e(N_e, \langle E_e\rangle) = N_e\langle E_e\rangle$$

$$= N_e \int_0^\infty E_e f_F(E_e; E^F, T_e) g(E_e; \Delta) dE_e. \tag{42}$$

By varying now (42) over N_e and $\langle E_e\rangle$ (i.e. assuming that these variables are independent), we obtain

$$\frac{dQ_e}{dt} = \langle E_e\rangle \frac{dN_e}{dt}\bigg|_{\langle E_e\rangle=\text{const}} + N_e \frac{d\langle E_e\rangle}{dt}\bigg|_{N_e=\text{const}}$$

$$= \frac{Q_e}{N_e}\frac{dN_e}{dt} - N_e\gamma_{ep}^{(Q)}\left[\langle E_e(E_F, T_e)\rangle - \langle E_e(E_F, T_p)\rangle\right] =$$

$$= P_p(t)\frac{\hbar\omega}{2} - \frac{Q_e}{N_e}\gamma_{ehp}^{(r)}\left(N_e^2 - N_s^2\right) - \gamma_{ep}^{(Q)}\left(Q_e - \frac{N_e}{N_{es}}Q_{es}\right). \tag{43}$$

Here, we used the relaxation approximation

$$\frac{d\langle E_e\rangle}{dt}\bigg|_{N_e=\text{const}} = -\gamma_{ep}^{(Q)}\left[\langle E_e(E^F, T_e)\rangle - \langle E_e(E^F, T_p)\rangle\right]$$

$$= -\gamma_{ep}^{(Q)}\left(\frac{Q_e}{N_e} - \frac{Q_{es}}{N_{es}}\right) \tag{44}$$

in a series of transformations, where $\gamma_{ep}^{(Q)}$ is the relaxation rate of $\langle E_e\rangle$ (in fact, of T_e), which is expressed within the framework of the two-temperature model [38] in terms of the specific heats $c_{e,p}$ of the electron and phonon subsystems of a HTSC sample depending on $T_{e,p}$;

$$Q_{es} = N_{es}\int_0^\infty E_e f_F(E_e; E^F, T_p) g(E_e; \Delta) dE_e,$$

$$N_{es} = N_c \int_0^\infty f_F(E_e; E^F, T_p) g(E_e; \Delta) dE_e$$

is the energy density and concentration of free electrons at the equilibrium temperature $T_e = T_p$, but at the non-equilibrium position $E^F \neq E_0^F$ of the Fermi level. The first term in the right-hand part of (44) takes into account the energy supply to the electronic subsystem due to the absorption of pump radiation, the second term describes the energy loss caused by phonon-assisted recombination, and, the third one describes the cooling of the electronic subsystem due to transfer of the kinetic energy of free carriers to the phonon subsystem. Equation (44) is written by assuming that the probability of the recombination process is independent of the energy of quasi-particles.

The energy exchange with a thermostat, whose role is played by a substrate at temperature T_s, is described by the kinetic equation for the energy density (heat storage) Q_p in the phonon subsystem. Taking into account the balance between the energy supply and loss and the principle of detailed balancing, this equation will take the form

$$\frac{dQ_p}{dt} = 2\frac{Q_e}{N_e}\gamma_{ehp}^{(r)}\left(N_e^2 - N_s^2\right)$$

$$+ 2\gamma_{ep}^{(Q)}(Q_e - Q_{es}) - \gamma_{ps}^{(Q)}(Q_p - Q_{ps}) \tag{45}$$

in the relaxation approximation. Here, we used the notation $Q_{p,ps} = c_p T_{p,ps}$, where T_p and T_{ps} are the current and equilibrium temperatures of the phonon subsystem, respectively. We can assume in calculations that due to the immense heat capacity of the thermostat (substrate), $T_s \equiv T_0$. Note that the rate constant $\gamma_{ps}^{(Q)}$ of relaxation of the heat excess in (45) can depend on T_p and T_s because the specific heat c_p of the phonon subsystem depends on temperature.

3.2 Kinetics of thermodynamic parameters upon femtosecond pumping

It was assumed in numerical calculations [59–61] that the initial conditions are determined by the values

$E^{\mathrm{F}}(t=0) = E_0^{\mathrm{F}} = 0$ and $T_{\mathrm{e}}(t=0) = T_0$ through the expressions

$$N_{\mathrm{e}}(t=0) = N_{\mathrm{c}} \int_0^{\infty} f_{\mathrm{F}}(E_{\mathrm{e}}; E^{\mathrm{F}}=0, T_{\mathrm{e}}=T_0) g(E_{\mathrm{e}}; \Delta) \mathrm{d}E_{\mathrm{e}}, \quad (46)$$

$$Q_{\mathrm{e}}(t=0) = N_{\mathrm{e}} \int_0^{\infty} E_{\mathrm{e}} f_{\mathrm{F}}(E_{\mathrm{e}}; E^{\mathrm{F}}=0, T_{\mathrm{e}}=T_0) \times g(E_{\mathrm{e}}; \Delta) \mathrm{d}E_{\mathrm{e}}, \quad (47)$$

$$Q_{\mathrm{p}}(t=0) = c_{\mathrm{p}} T_0. \quad (48)$$

The energy gap Δ in the electronic spectrum of a HTSC was assumed a constant depending only on the initial temperature T_0 and the superconducting transition temperature T_{c} (see section 2):

$$\Delta = \Delta(T_0) \equiv \begin{cases} 3.12 k_{\mathrm{B}} T_{\mathrm{c}} \left(1 - \dfrac{T_0}{T_{\mathrm{c}}}\right)^{1/2} & \text{for } T_0 \leqslant T_{\mathrm{c}}, \\ 0 \text{ for } T_0 > T_{\mathrm{c}}. \end{cases} \quad (49)$$

Expression (49) corresponds to the so-called weak coupling limit in the BCS theory. The instant values of $E^{\mathrm{F}}(t)$ and $T_{\mathrm{e}}(t)$ were determined by solving the system of integral equations

$$N_{\mathrm{e}}(t \neq 0) = N_{\mathrm{c}} \int_0^{\infty} f_{\mathrm{F}}(E_{\mathrm{e}}; E^{\mathrm{F}}, T_{\mathrm{e}}) g(E_{\mathrm{e}}; \Delta) \mathrm{d}E_{\mathrm{e}}, \quad (50)$$

$$Q_{\mathrm{e}}(t \neq 0) = N_{\mathrm{e}} \int_0^{\infty} E_{\mathrm{e}} f_{\mathrm{F}}(E_{\mathrm{e}}; E^{\mathrm{F}}, T_{\mathrm{e}}) g(E_{\mathrm{e}}; \Delta) \mathrm{d}E_{\mathrm{e}}. \quad (51)$$

The distribution of the electronic state density $g(E_{\mathrm{e}}; \Delta \equiv 0)$ for $T_0 > T_{\mathrm{c}}$ was calculated from the standard expression [93]

$$g(E_{\mathrm{e}}; \Delta \equiv 0) = \frac{1}{4\pi^3} \oiint_{E_{\mathrm{e}}=\mathrm{const}} \frac{\mathrm{d}S}{|\nabla_k E_{\mathrm{e}}(\boldsymbol{k})|} \quad (52)$$

taking into account the data on $E_{\mathrm{e}}(\boldsymbol{k}_{\mathrm{e}})$, i.e. the 'real' (calculated by the pseudopotential method) zone structure of La_2CuO_4 [100] (Fig. 9a). Here, $E_{\mathrm{e}}(\boldsymbol{k}_{\mathrm{e}})$ describes the shape of the conduction band of La_2CuO_4, i.e. the dependence of the electronic energy E_{e} on the quasi-momentum $\boldsymbol{k}_{\mathrm{e}}$, while integral (52) is taken over the constant energy surface $E_{\mathrm{e}} = \mathrm{const}$. Upon integration, the data from [100] were interpolated to the first Brillouin zone by the method described in [66] taking symmetry into account. As expected, the calculated dependence $g(E_{\mathrm{e}}; \Delta \equiv 0)$ had the distinct peak of the state density in the vicinity of the point $E_{\mathrm{e}} = 0$. Then, this dependence in the range $|E_{\mathrm{e}} - E_0^{\mathrm{F}}| \leqslant 1$ eV was approximated by a smooth analytic function with an accuracy of 0.5 %. For $T_0 \leqslant T_{\mathrm{c}}$, we introduced compulsorily a gap of symmetry s into the obtained distribution $g(E_{\mathrm{e}}; \Delta \equiv 0)$, i.e. the states with energy E_{e} in a layer of thickness $2\Delta(T_0)$ in the vicinity of E_0^{F} were redistributed over the Brillouin zone according the expression

$$g(E_{\mathrm{e}}; \Delta) = \quad (53)$$

$$\begin{cases} 0 \text{ for } E_{\mathrm{e}} < \Delta, \\ g(E_{\mathrm{e}}; \Delta \equiv 0) + \dfrac{1}{k_{\mathrm{B}} T_0} \exp\left(-\dfrac{E_{\mathrm{e}}}{k_{\mathrm{B}} T_0}\right) \displaystyle\int_0^{\Delta(T_0)} g(E_{\mathrm{e}}; \Delta \equiv 0) \mathrm{d}E_{\mathrm{e}} \text{ for } E_{\mathrm{e}} \geqslant \Delta. \end{cases}$$

The evolution of the calculated distribution of the density of electronic states $\mathrm{DOS} = g(E_{\mathrm{e}}; \Delta)$ with changing T_0 is illustrated in Fig. 9b, where the instant of the appearance of the energy gap at the point $T_0 = T_{\mathrm{c}}$ is clearly observed.

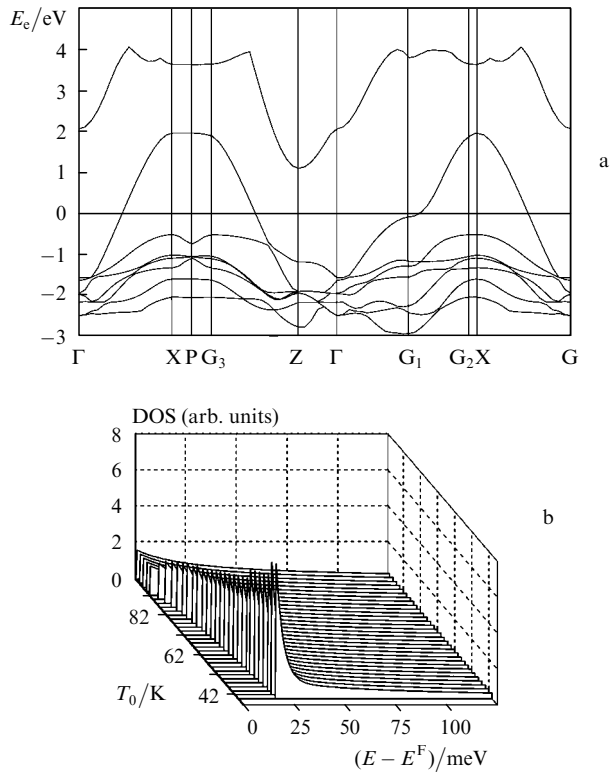

Figure 9. Band structure of La_2CuO_4 at room temperature [100] (a) and the distribution of the density of electronic states $\mathrm{DOS} = g(E_{\mathrm{e}}; \Delta)$ in the HTSC spectrum with changing the initial temperature T_0 (b).

The system of kinetic equations (35), (43), (45) was solved by the fourth-order Runge–Kutta method. The value of parameters corresponded to the standard conditions of most of the real experiments. It was assumed that a $\sim$ 200-nm HTSC film absorbs 30 % of the total energy (4×10^{-7} J) of the 800-nm, 30-fs pump pulse from a Ti : sapphire laser. The focal spot diameter was assumed to be 150 μm, while the rest of the parameters (the superconducting transition temperature $T_{\mathrm{c}} = 90$ K, heat capacity $c_{\mathrm{p}} = 0.9$ J cm^{-3} K^{-1}, heat escape rate to a substrate $\gamma_{\mathrm{ps}}^{(Q)} = 5 \times 10^{-3}$ ps^{-1}, and $E_{\max} = 15$ meV) were approximately equal to the parameters of a $YBa_2Cu_3O_{7-\delta}$ film on a $SrTiO_3$ substrate. The two remaining free parameters $\tilde{\gamma}_{\mathrm{ehe}}^{(\mathrm{r})}$ and $\tilde{\gamma}_{\mathrm{ehp}}^{(\mathrm{r})}$ were varied to obtain the calculated relaxation time τ_{r}' of the nonlinear response (see section 4) equal to ~ 0.3 and 1.5 ps for $T_0 = 100$ and 40 K, respectively, which is close to experimental values.

Figure 10 shows the transformation of kinetics of the shift $\Delta E^{\mathrm{F}}(t) = E_{\mathrm{e}}^{\mathrm{F}}(t) - E_0^{\mathrm{F}}$ of the Fermi level and changes in the electron temperature $\Delta T_{\mathrm{e}}(t) = T_{\mathrm{e}}(t) - T_0$, the total

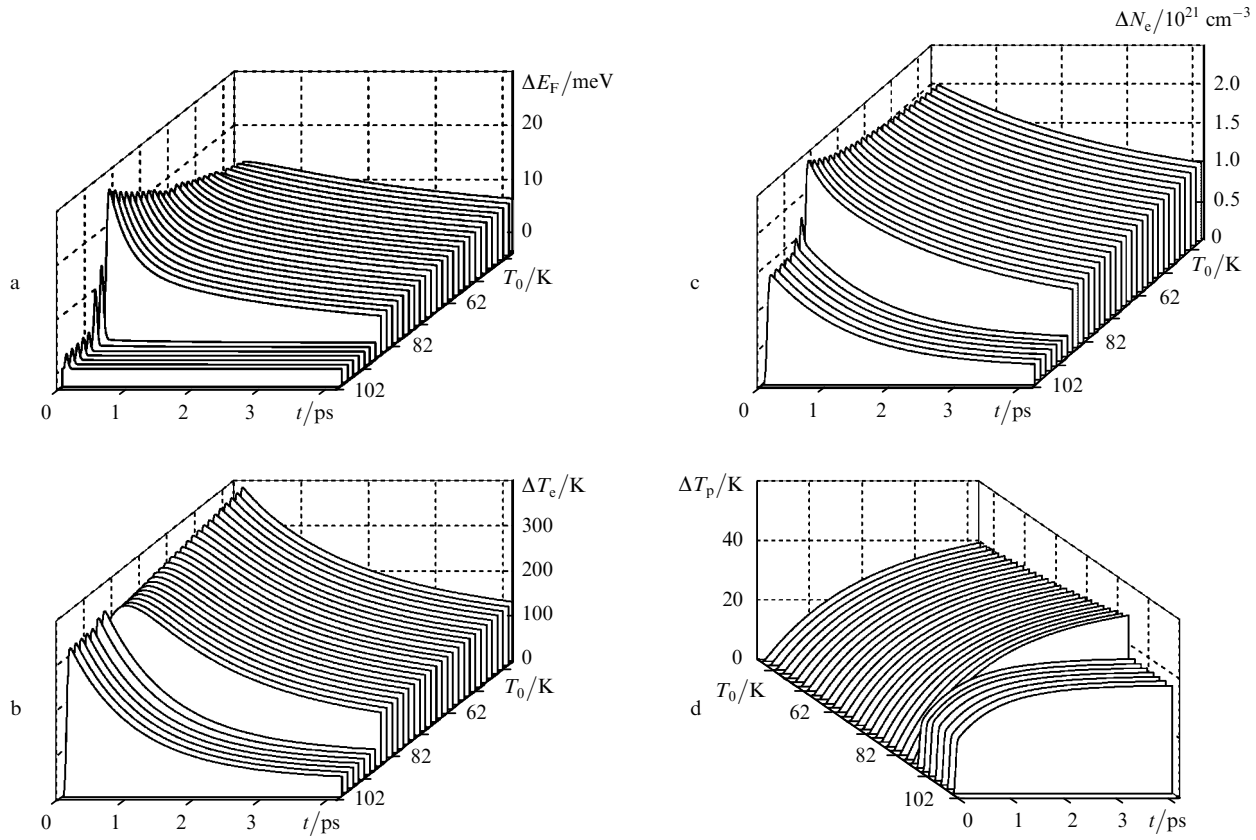

Figure 10. Transformation of kinetics $\Delta E^F(t) = E_e^F(t) - E_0^F$ (a), $\Delta T_e(t) = T_e(t) - T_0$ (b), $\Delta N_e(t) = N_e(t) - N_0$ (c), and $\Delta T_p(t) = T_p(t) - T_0$ (d) with changing T_0 for a HTSC film excited by a 30-fs pulse.

concentration $\Delta N_e(t) = N_e(t) - N_0$ of free carriers in the split part of the conduction band, and the lattice temperature $\Delta T_p(t) = T_p(t) - T_0$ depending of the initial temperature T_0 of the HTSC film. One can see that the absorption of pump radiation drastically changes the kinetics of thermodynamic parameters upon variations of T_0 in the vicinity of the point $T_0 \simeq T_c$ (the gap 'opening' point). The type of changes in the kinetics of the rate constants $\gamma_{ehe}^{(r)}(t)$ and $\gamma_{ehp}^{(r)}(t)$ of pair recombination upon variations of T_0 [59] proves the principal role of these processes.

3.3 Kinetics of thermodynamic parameters upon picosecond pumping

The kinetics of thermodynamic parameters of a HTSC film upon picosecond excitation [61] was simulated similarly. The system of kinetic equations (35), (43), (45) was solved by assuming that the duration τ_{pulse} of the pump pulse of the same energy (4×10^{-7} J) was 20 ps, while the rest of the control parameters were the same. The energy gap in the electronic spectrum was assumed 'frozen', as before, and the rate constants $\tilde{\gamma}_{ehe}^{(r)}$ и $\tilde{\gamma}_{ehp}^{(r)}$ of nonradiative three-body recombination in (36) and (39) were taken from calculations described above.

Figure 11 illustrates the transformation of the calculated kinetics of the instant shift $\Delta E_F(t) = E_e^F(t) - E_0^F$ of the Fermi level with respect to its initial position and also of the jump $\Delta T_e(t) = T_e(t) - T_0$ of the electron temperature of the HTSC film upon variations of its initial temperature. It is easy to verify that even under conditions of a relatively slow picosecond excitation of a sample, the amplitude of

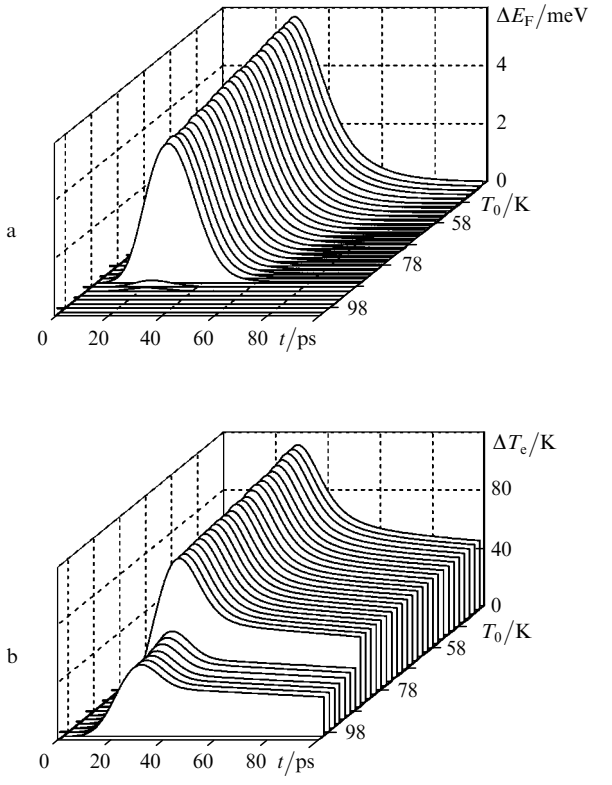

Figure 11. Transformation of kinetics $\Delta E^F(t) = E_e^F(t) - E_0^F$ (a) and $\Delta T_e(t) = T_e(t) - T_0$ (b) with changing T_0 for a HTSC film excited by a 20-ps pulse.

instant deviations of its thermodynamic parameters from equilibrium values drastically increases after the opening of the energy gap in the electronic spectrum (upon passage through the point $T_0 \simeq T_e$).

4. Nonlinear HTSC response

4.1 Electronic part of a nonlinear response upon one-photon probing

First we consider the nonlinear response of a HTSC film in the classical version of the pump–probe method with one-photon probing of the excited state by a probe pulse at the wavelength λ, i.e. we will study the kinetics of variations in the reflection (ΔR) and transmission (ΔT) coefficients of the sample after the absorption of the pump pulse. We assume, as in [59, 61], that the nonlinear response of the HTSC film is determined by a change $\delta\varepsilon(\lambda, T_0)$ in its initial complex dielectric constant $\varepsilon_0 = \varepsilon(\lambda, T_0)$ caused by the deviation of thermodynamic parameters E_e^F and T_e from their equilibrium values. Because the reflection coefficient $R(\lambda, T_0)$ at the air–HTSC film interface is determined by the dielectric constant ε of the latter according to the expression

$$R(\lambda, T_0) = \left[\frac{\varepsilon^{1/2}(\lambda, T_0) - 1}{\varepsilon^{1/2}(\lambda, T_0) + 1}\right]^2, \tag{54}$$

by varying it by the substitution $R(\lambda, T_0) = R_0(\lambda, T_0) + \delta R(\lambda, T_0)$ and $\varepsilon(\lambda, T_0) = \varepsilon_0(\lambda, T_0) + \delta\varepsilon(\lambda, T_0)$ and restricting ourselves to the first correction to the initial reflection coefficient $R_0(\lambda, T_0)$ in $\delta\varepsilon(\lambda, T_0)$, we obtain

$$\delta R(\lambda, T_0) = 2R_0(\lambda, T_0)\,\frac{\delta\varepsilon(\lambda, T_0)}{\varepsilon_0^{1/2}(\lambda, T_0)[\varepsilon_0(\lambda, T_0) - 1]}. \tag{55}$$

In fact, such an approach is always used to interpret the data obtained in any real experiment. However, unlike papers [18, 19, 21, 27, 30–34, 48, 52, 53], where absorption of light by free carriers (excited by the pump pulse) was taken into account during probing, we will calculate $\delta\varepsilon$ taking into account the electronic part of the instant linear response ε of the HTSC film caused only by interband transitions. In principle, the authors of papers [20, 22, 47] attempted earlier to realise a similar procedure; however, it will be clear below that our models are more accurate and realistic.

The value of $\delta\varepsilon(\lambda, T_0)$ was calculated in two spectral intervals $\lambda \sim 800$ and 620–680 nm by using the standard expression

$$\varepsilon \sim \sum_{i \neq i'} \int\int \frac{\left|d_{i,i'}(\boldsymbol{k}_e, \boldsymbol{k}_e')\right|^2 n_i(\boldsymbol{k}_e)\left[1 - n_{i'}(\boldsymbol{k}_e')\right]}{\omega - \Omega_{i,i'}(\boldsymbol{k}_e, \boldsymbol{k}_e') + i\Gamma_{i,i'}(\boldsymbol{k}_e, \boldsymbol{k}_e')}\,d\boldsymbol{k}_e\,d\boldsymbol{k}_e'. \tag{56}$$

Here, $\boldsymbol{k}_e$ is the electron quasi-momentum; the subscripts i and i' number electronic state bands involved in the $(i, \boldsymbol{k}_e) \to (i', \boldsymbol{k}_e')$ transition with the dipole moment $d_{i,i'}(\boldsymbol{k}_e, \boldsymbol{k}_e')$; $n_i(\boldsymbol{k}_e)$ is the occupation number of the $(i, \boldsymbol{k}_e)$ state, which is determined by the Fermi–Dirac distribution; ω is the probe frequency; $\Omega_{i,i'}(\boldsymbol{k}_e, \boldsymbol{k}_e')$ is the resonance frequency of the $(i, \boldsymbol{k}_e) \to (i', \boldsymbol{k}_e')$ transition; and $\Gamma_{i,i'}(\boldsymbol{k}_e, \boldsymbol{k}_e')$ is the relaxation rate of interband polarisation. Integration over $\boldsymbol{k}_e$ and $\boldsymbol{k}_e'$ is performed within the first Brillouin zone, and summation over the subscripts i and i' includes all the bands of allowed electronic states.

In the case of one-photon probing, taking into account that the photon momentum is small compared to $\boldsymbol{k}_e$, the $(i, \boldsymbol{k}_e) \to (i', \boldsymbol{k}_e')$ transitions can be considered direct ($\boldsymbol{k}_e = \boldsymbol{k}_e'$) and we can pass in (56) to single integration over $\boldsymbol{k}_e$ by using the notation $d_{i,i'}(\boldsymbol{k}_e, \boldsymbol{k}_e') = d_{i,i'}(\boldsymbol{k}_e)$, $\Gamma_{i,i'}(\boldsymbol{k}_e, \boldsymbol{k}_e') = \Gamma_{i,i'}(\boldsymbol{k}_e)$, and $\Omega_{i,i'}(\boldsymbol{k}_e, \boldsymbol{k}_e') = \Omega_{i,i'}(\boldsymbol{k}_e)$. After that, the resonance frequencies in (56) will be determined by standard expressions $\Omega_{i,i'}(\boldsymbol{k}_e) = E_{i'}(\boldsymbol{k}_e) - E_i(\boldsymbol{k}_e)$, where $E_i(\boldsymbol{k}_e)$ is the electron energy in the (i, $\boldsymbol{k}_e$) state normalised to Planck's constant.

As in [64, 67], we assumed in numerical calculations that $d_{i,i'}(\boldsymbol{k}_e) = d$ and $\Gamma_{i,i'}(\boldsymbol{k}_e) = \Gamma = 5 \times 10^{12}\ s^{-1}$ are constants independent of i, i', and $\boldsymbol{k}_e$. Frequencies $\Omega_{i,i'}(\boldsymbol{k}_e)$ were found by interpolating the data [100] on the band structure of La_2CuO_4 at room temperature to the first Brillouin zone taking into account the requirements of symmetry and periodicity [66]. Cooling down to temperatures $T_0 \leqslant T_c$ was simulated by the compulsory introduction of a frozen energy gap (49) into the obtained electronic spectrum, i.e. by the replacement $E_e(\boldsymbol{k}_e) \to E_0^F \pm \{[E_e(\boldsymbol{k}_e) - E_0^F]^2 + \Delta(T_0)^2\}^{1/2}$ for $E_e(\boldsymbol{k}_e) > E_0^F$ and $E_e(\boldsymbol{k}_e) < E_0^F$, respectively [59–61]. As a result, the electronic state density in the vicinity of the Fermi level was redistributed, imitating the phase transition. Both procedures described above allowed us to include the real electronic spectrum (i.e. known from the literature) to our model, thereby drastically reducing the number of fitting parameters. Integration in expression (56) was performed by the special point method [101] over the state bands lying in the energy range $|E_e \pm E_0^F| \leqslant 2.5$ eV.

The dielectric constant $\varepsilon_0(\lambda, T_0)$ was calculated (in the absence of pumping) by assuming that the occupation numbers $n_i(\boldsymbol{k}_e)$ in (56) were specified by the Fermi–Dirac distribution $f_F(E_e; E_0^F, T_0)$. Upon femtosecond excitation of the HTSC film, the occupation numbers $n_i(\boldsymbol{k}_e)$ at each instant of time t were determined from the Fermi–Dirac distribution $f_F(E_e; E_e^F, T_e)$ with the instant values of thermodynamic parameters $E_e^F(t)$ and $T_e(t)$ calculated by the method described in section 3 (see Fig. 10). Upon picosecond excitation, $n_i(\boldsymbol{k})$ were assumed to be specified by the Fermi–Dirac distribution with the thermodynamic parameters $\langle E_e^F \rangle_t$ и $\langle T_e \rangle_t$ averaged over the pump pulse duration $\tau_{pulse} = 20$ ps (see Fig. 11). This simulated the situation with pump–probe instants coincident in time, which corresponds to saturation spectroscopy experiments.

4.2 Nonlinear HTSC response upon two-photon probing

The state of a HTSC sample in BP [9, 25, 26, 56, 64] and DFPS [10, 11, 37, 64, 67] methods is probed by two photons by using two probe pulses at wavelengths $\lambda_{1,2}$ (at frequencies $\omega_{1,2}$) that coincide in time but propagate at an angle to each other (with the wave vectors $\boldsymbol{k}_1 \neq \boldsymbol{k}_2$). Experimentally, the self-diffraction efficiency η (the efficiency of filed generation in the direction $\boldsymbol{k}_3 = 2\boldsymbol{k}_1 - \boldsymbol{k}_2$ at frequency $\omega_3 = 2\omega_1 - \omega_2$) is measured as a function of the frequency detuning $\Delta\omega = \omega_1 - \omega_2$ of the BP components or of the wavelength λ of probe pulses when their frequencies coincide ($\omega_1 = \omega_2$, DFPS).

The nonlinear response in this case can be described within the framework of the model developed in [9, 66]. This model assumes that the total cubic nonlinear susceptibility χ of a sample contains several components:

$$\chi = \chi_r + \chi_{nr} + \chi_s + \chi_0. \quad (57)$$

Here, χ_r and χ_{nr} are the resonance and nonresonance (see below) parts of the electronic response caused by interband transitions; χ_s is the susceptibility component related to scattering by acoustic phonons; χ_0 is a constant caused by errors of the model and, first of all, by a finiteness of the integration region over the initial and final electronic states. The restriction of the integration region in calculations inevitably leads to errors in the description of nonresonance processes caused by transitions to the bands that were neglected, absorption by free carriers, etc.

The nonresonance part χ_{nr} can be calculated by using the approach developed in [9, 66]. In this case, it is sufficient to take into account in the cubic nonlinear susceptibility of a HTSC sample the contributions from all one- and two-photon resonance electronic transitions in the real (calculated from the same data [100]) electronic spectrum and their real (calculated from the same kinetic data for E_e^F and $T_{e,p}$) occupation numbers. In this case, the expression for χ_{nr} takes the form [9, 66]

$$\chi_{nr} \propto P_0\{K_+P_+ + K_-P_-\}, \quad (58)$$

which is standard for nonlinear optics and spectroscopy [102], where

$$P_0 = \sum_{i,i'} \int\int \frac{|d_{i,i'}(\boldsymbol{k}_e, \boldsymbol{k}'_e)|^2 n_i(\boldsymbol{k}_e)[1 - n_{i'}(\boldsymbol{k}'_e)]}{[\omega_1 - \Omega_{i,i'}(\boldsymbol{k}_e, \boldsymbol{k}'_e) - i\Gamma_{i,i'}(\boldsymbol{k}_e, \boldsymbol{k}'_e)]^2} \, d\boldsymbol{k}_e \, d\boldsymbol{k}'_e, \quad (59)$$

$$P_\pm = \sum_{i,i'} \int\int \frac{|d_{i,i'}(\boldsymbol{k}_e, \boldsymbol{k}'_e)|^2 n_i(\boldsymbol{k}_e)[1 - n_{i'}(\boldsymbol{k}'_e)]}{[\omega_1 \pm \Delta\omega - \Omega_{i,i'}(\boldsymbol{k}_e, \boldsymbol{k}'_e) \pm i\Gamma_{i,i'}(\boldsymbol{k}_e, \boldsymbol{k}'_e)]^2} \, d\boldsymbol{k}_e \, d\boldsymbol{k}'_e, \quad (60)$$

$$K_\pm = \sum_{i,i'} \int\int \frac{|d_{i,i'}(\boldsymbol{k}_e, \boldsymbol{k}'_e)|^2 n_i(\boldsymbol{k}_e)[1 - n_{i'}(\boldsymbol{k}'_e)]}{\pm\Delta\omega + \Omega_{i,i'}(\boldsymbol{k}_e, \boldsymbol{k}'_e) \pm i\Gamma_{i,i'}(\boldsymbol{k}_e, \boldsymbol{k}'_e)} \, d\boldsymbol{k}_e \, d\boldsymbol{k}'_e, \quad (61)$$

and all other notations are the same as in the previous section.

We calculated χ_{nr} by using the same approximations [$\boldsymbol{k}_e = \boldsymbol{k}'_e$, $d_{i,i'}(\boldsymbol{k}, \boldsymbol{k}') = d$, and $\Gamma_{i,i'}(\boldsymbol{k}, \boldsymbol{k}') = \Gamma = \text{const}$], procedures for determining $\Omega_{i,i'}(\boldsymbol{k}_e, \boldsymbol{k}'_e)$ and integration as for one-photon probing, as well as the replacement $E_e(\boldsymbol{k}_e) \to E_0^F \pm \{[E_e(\boldsymbol{k}_e) - E_0^F]^2 + \Delta(T_0)^2\}^{1/2}$ for $E_e(\boldsymbol{k}_e) \geqslant E_0^F$ and $E_e(\boldsymbol{k}_e) < E_0^F$ simulating cooling. The frequency detuning in the DFPS method was assumed zero ($\Delta\omega \equiv 0$, $\lambda = \lambda_1 \equiv \lambda_2$), and the probe wavelength was changed (frequency $\omega = \omega_1 \equiv \omega_2$). In the BP method, the point of coincidence of frequencies was fixed ($\lambda = \lambda_1 = \lambda_2 = \text{const}$ for $\Delta\omega = 0$), while the frequency ω_2 of one of the BP components was tuned ($\Delta\omega \neq 0$). In the femtosecond pump–probe method, the occupation numbers $n_i(\boldsymbol{k}_e)$ at each instant t were assumed to be determined by the Fermi–Dirac distribution $f_F(E_e; E_e^F, T_e)$ with the instant values of thermodynamic parameters $E_e^F(t)$ and $T_e(t)$ calculated by the method described in section 3 (see Figs 10a, b). In the case of picosecond excitation, we assumed that the occupation numbers $n_i(\boldsymbol{k})$ were specified by the Fermi–Dirac distribution with the values of thermodynamic parameters $\langle E_e^F \rangle_t$ и $\langle T_e \rangle_t$ averaged over the pump pulse duration $\tau_{pulse} = 20$ ps (see Fig. 11), which again simulated the situation with pump and probe pulses made coincident in time.

The only fitting parameter in the calculation of χ_{nr} is the relaxation rate Γ of interband polarisation, whose value (150 cm^{-1}) was selected to obtain the best agreement between the calculated width of spectral features of the nonlinear response in the DFPS method and the width observed in one-photon probing experiments [22, 47] and was not varied then.

The approximation $\boldsymbol{k}_e = \boldsymbol{k}'_e$ used in the calculation of χ_{nr} results in the loss of contributions introduced by two-photon resonance transitions $\boldsymbol{k}_e \to \boldsymbol{k}'_e$ between the states separated by the energy gap within one band. Taking into account the condition $\boldsymbol{k}'_e = \boldsymbol{k}_e + \boldsymbol{k}_1 - \boldsymbol{k}_2$ (the law of conservation of momentum), the role of such transitions will be significant for states within a narrow vicinity ($|\boldsymbol{k}_e| \leqslant |\boldsymbol{k}_e^F| - |\boldsymbol{k}_1 - \boldsymbol{k}_2|$ of the Fermi surface for $\Delta\omega \sim 2\Delta(T_0)$. It is this circumstance that is reflected by the term the nonresonance part of an electronic nonlinear response that we introduced for χ_{nr}. However, because of a drastic increase in the state density near the Fermi surface, the role of transitions of this type in a HTSC can be rather important. Because of this, the resonance component χ_r was introduced into nonlinear response (57) to take into account the corresponding contributions. The value of χ_r was calculated within the framework of the effective two-level system [103], i.e. the anisotropy of the band structure was neglected and integration in (59)–(61) was performed over energy E_i taking into account the condition $E_{i'} - E_i = 2\Delta(T_0)$, similarly to the approach described in section 2 and [59]. As a result, the weight of χ_r with respect to χ_{nr} was not determined unambiguously and was considered below as another fitting parameter. Its value was found to provide the agreement between the calculated and experimental [56] dependences $\eta(\Delta\omega) \propto |\chi(\Delta\omega)|^2$ in the BP method and was assumed equal to 0.075 at $T_0 = 90$ K and proportional to T_0^2. The latter took into account an increase in the amplitude and steepness of the state density peak with decreasing T_0. Note also that the value of χ_r was calculated by assuming that the relaxation rate of interband polarisation was lower ($\Gamma = 50$ cm^{-1}) than that for χ_{nr} (see above) because only in this case the spectral features of the dependence $\eta(\Delta\omega)$ were consistent with experimental data [56]. This is not surprising in principle because the relaxation rate should decrease near the edges of the allowed state bands [32, 38, 47].

The contribution of processes involving acoustic phonons was calculated from the expression

$$\chi_s = -\frac{\chi_{ac}}{(\Delta\omega)^2 + (4\delta\omega)^2 + i4\delta\omega\Delta\omega}, \quad (62)$$

which follows from the usual relation for nonlinearity of the Mandelstam–Brillouin type [104] convoluted with the spectra of two pulses exciting sound taking into account that τ_{pulse} is much shorter than the decay time of the latter. In the case of femtosecond pulses, the contribution of term (62) into total response (57) can be neglected. The picosecond spectroscopy data were simulated by assuming that the spectral width was $\delta\omega = 1.5$ cm^{-1}, in accordance with the experimental width [25, 56]. As a result, the component χ_s contained one free parameter – the complex amplitude χ_{ac}, which was assumed proportional to T_0 due

to an increase in the occupation numbers of acoustic phonon modes with increasing the initial temperature.

The dependence $\chi(\Delta\omega, T_0)$ in the BP method was simulated numerically by assuming that both pump components have the wavelength 625 nm at the frequency-coincidence point ($\Delta\omega = 0$), i.e. they are localised in the spectral region where the electronic part of the nonlinear response of a HTSC sample is small both in experiments [22, 47] and theoretically [59–61, 67]. The results of calculations were fitted by using two parameters. The amplitude χ_{ac} of the component χ_s and also χ_0 were selected so that due to the interference of all contributions to χ, the dependence of the self-diffraction efficiency $\eta(\Delta\omega, T_0) \propto |\chi(\Delta\omega, T_0)|^2$ had 'holes' at the points $\Delta\omega = 10\ \mathrm{cm}^{-1}$ at $T_0 \simeq 90$ K and $\Delta\omega = 63\ \mathrm{cm}^{-1}$ at $T_0 = 80$ K, in accordance with experimental data [26]. Note, however, that the point $\Delta\omega = 0$ in [26] was slightly shifted (to $\lambda \simeq 620.4$ nm). The dependences $\eta(\lambda, T_0) \propto |\chi(\lambda, T_0)|^2$ measured by the DFPS method were already calculated without any fitting, by using the same expressions (57)–(62) and procedures and the values of χ_{ac} and χ_0 that were found as described above.

5. Numerical simulations of a nonlinear response

5.1 One-photon femtosecond probing

First we consider the results of simulation of the kinetics of the nonlinear response $\delta\varepsilon(\lambda, T_0)$ of a HTSC film for two modifications of the pump–probe method with one-photon femtosecond excited-state probing [59]. We will assume that the thermodynamic parameters E_e^F and T_e of the electronic subsystem of a sample with the same characteristics (see section 3) change in time due to absorption of 30 % of the total energy (4×10^{-7} J) of a 800-nm, 30-fs pulse focused to a spot of diameter 150 μm on a ~200-nm thick film. However, in the first of the considered situations (see Fig. 12), we will assume that the instant state of the film is probed by a pulse at the same wavelength (800 nm), i.e. we will simulate the experimental data that are similar to those obtained in [18, 19, 21, 30–34, 48, 52, 53]. Then (see Fig. 13), we will assume that a different experimental situation is realised and the state of the sample is probed by a short pulse of the same duration in the range from 620 to 680 nm (for example, by a broadband supercontinuum pulse), which corresponds to experimental conditions described in [20, 22, 47]. This modification of the pump–probe method is often called spectrochronography [105].

Figure 12a illustrates the transformation of the calculated kinetics of changes in the modulus of the dielectric constant $\Delta\varepsilon(t) = |\varepsilon(t)| - |\varepsilon_0|$ of the HTSC film upon variations of T_0 and one-photon probing at a wavelength of 800 nm. The exponential approximation of the initial (with small probe-pulse delays) part of the family of kinetic curves $\Delta\varepsilon(t, T_0)$ presented here gives a nontrivial dependence of the relaxation time $\tau_{\Delta\varepsilon}$ of the nonlinear response on T_0 (Fig. 12b) with a distinct abrupt step (the jump of $\tau_{\Delta\varepsilon}$ at $T_0 \simeq 86$ K, which is slightly lower than the phase transition temperature $T_c = 90$ K). It is easy to see that both the transformation of the dependence $\Delta\varepsilon(t)$ (Fig. 12a) with changing T_0 (the presence of the region of two-exponential relaxation of $\Delta\varepsilon$ at T_0 in the vicinity of the point $T_c = 90$ K) and the calculated dependence $\tau_{\Delta\varepsilon}(T_0)$ itself (Fig. 12b) are in good agreement with the experimental kinetics of the

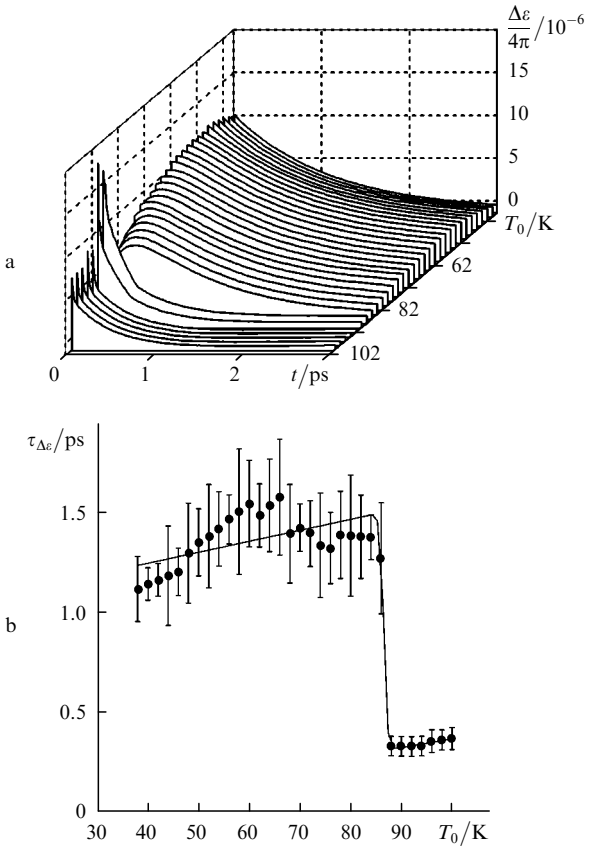

Figure 12. Transformation of the kinetics $\Delta\varepsilon(t) = |\varepsilon(t)| - |\varepsilon_0|$ upon one-photon femtosecond probing at a wavelength of 800 nm and variations of the initial temperature T_0 (a) and the dependence of the relaxation time $\tau_{\Delta\varepsilon}$ on T_0 (b).

nonlinear response observed in experiments [32, 34, 41, 48, 52, 53] (see section 1). The only feature of the dependence $\tau_{\Delta\varepsilon}(T_0)$ that was lost in the simulation is the absence of a narrow peak of $\tau_{\Delta\varepsilon}$ at the top of the 'step' (Fig. 12b). This is most likely explained by the use of the approximation according to which the rates of relaxation processes in (35), (43)–(45) depend only on mean energies. Note also that all the above-mentioned 'anomalies' of the nonlinear response kinetics disappear with decreasing the pump-pulse energy (when $E_{e,h}^F$ coincides with E_0^F).

Upon one-photon probing of the kinetics of the excited state of the HTSC by a femtosecond supercontinuum pulse, the situation becomes more complicated. Figure 13 shows the calculated spectral dependences of the change in the modulus of the dielectric constant $\Delta\varepsilon(\lambda) = |\varepsilon(\lambda)| - |\varepsilon_0|$ of the HTSC film produced by the same pump pulse in the wavelength range from 620 to 680 nm at $T_0 = 100$ and 40 K and different probe-pulse delays ($t = 30$ fs, 1, 2, 3, and 7 ps). Although $\tau_{\Delta\varepsilon}$ also experiences a jump with decreasing T_0 down to the same value $T_0 \simeq 86$ K and a step is formed in the dependences $\tau_{\Delta\varepsilon}(T_0)$ for all λ, nevertheless due to a continuous displacements of the local extrema of $\Delta\varepsilon(\lambda)$ with increasing t, the further run of curves $\tau_{\Delta\varepsilon}(T_0)$ in the low-temperature region ($T_0 < 86$ K) depends on λ (Fig. 14b). As in experiments [20, 22, 47], there exist points on the wavelength axis at which $\Delta\varepsilon \equiv 0$. These points separate spectral regions with the opposite signs of changes $\Delta\varepsilon$ induced by the pump pulse (Fig. 13b). Note that this result is not such trivial as it may seem, because we are dealing with the

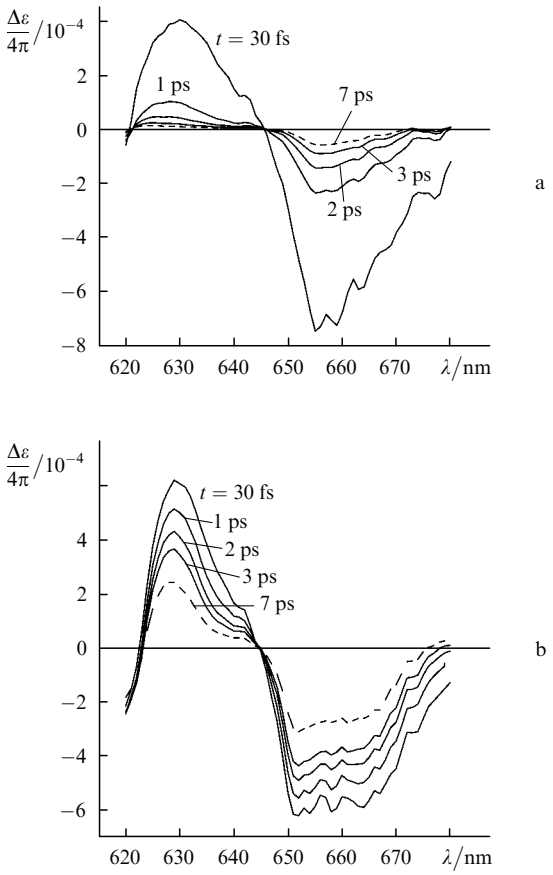

Figure 13. Spectral dependence $\Delta\varepsilon(\lambda) = |\varepsilon(\lambda)| - |\varepsilon_0(\lambda)|$ in the case of one-photon femtosecond probing in the range 620–680 nm for $T_0 = 100$ (a) and 40 K (b) and different delay times t of the probe pulse.

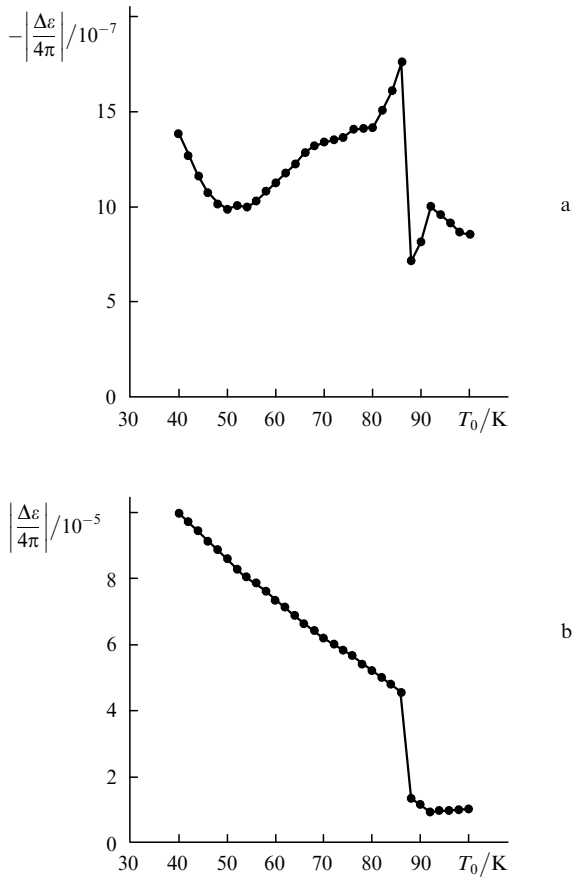

Figure 14. Dependences of $\Delta\varepsilon = |\varepsilon| - |\varepsilon_0|$ on T_0 upon one-photon picosecond probing ($\tau_{\text{pulse}} = 20$ ps) of changes at the wavelengths 800 (a) and 625 nm (b) induced by the pump pulse.

simultaneous vanishing of the real and imaginary parts of the nonlinear response. Therefore, in our opinion, the presence of such points on the wavelength axis can be caused only by a change in the phase relations between two interfering components of $\delta\varepsilon$ and is related to the frequency degeneracy of probing [67].

5.2 One-photon picosecond pumping-probing

Recall (see section 4) that in this case the situation with 20-ps pump and one-photon probe pulses coincident in time was simulated (i.e. the results of simulation should correspond to the results of saturation spectroscopy measurements). Figure 14 illustrates the jump of the amplitude of changes in the modulus of the dielectric constant $\Delta\varepsilon$ of the HTSC induced by the pump pulse upon variations of T_0 in the vicinity of the phase transition point $T_0 \simeq T_e$ and probing at 800 and 625 nm. One can see that the signs of $\Delta\varepsilon$ in these two situations are opposite. This means that in this case, there also exist points with $\Delta\varepsilon \equiv 0$, which separate spectral regions with the opposite signs of pump-induced variations $\Delta\varepsilon$. At the same time, it is unlikely that the corresponding measurements can be performed in practice because the amplitude of variations in ε caused the pump pulse is too small in this case.

5.3 Two-photon femtosecond probing

The main advantage of two-photon probing methods (BP and DFPS methods) is a drastic reduction of the initial background level. This is achieved because in this case the energy characteristics of light pulses are measured, which are produced exclusively by nonlinear processes (self-diffraction) [9–11, 25, 26, 56].

Note at once that the results presented below differ from those reported in [67] because calculations performed in [67] neglected the shift of the Fermi level (degeneracy), whose role, as shown above, proved to be quite important.

Figure 15 shows the transformation of the dependence of the modulus of the nonlinear response $\chi(\lambda)$ of the HTSC upon frequency-degenerate ($\lambda = \lambda_{1,2}$, $k_1 \neq k_2$) two-photon femtosecond probing of the excited state of the HTSC in the wavelength range from 620 to 680 nm at $T_0 = 100$, 90, 76, and 40 K for probing instants $t = 30$ fs, 0.5, 1.5, and 2.0 ps. In experiments, a differential measurement scheme is often used when the two situations are compared: in the presence of the pump pulse (χ for $E_{e,h}^F \neq E_0^F$, $T_{e,h} \neq T_0$) and in its absence (χ_0 for $E_{e,h}^F \equiv E_0^F$, $T_{e,h} \equiv T_0$). The calculated dependences of the difference $\Delta\chi = |\chi| - |\chi_0|$ on λ for $T_0 = 100$, 90, 76, and 40 K and the same probe-pulse delays are presented in Figs 16a–d. One can see that, as in the case of one-photon probing of changes induced by the pump pulse (see above), there also exists a point ($\Delta\chi \equiv 0$) on the wavelength axis separating regions with the opposite signs of $\Delta\chi$ (see Figs 16a–d).

The exponential approximation of the decay kinetics of $\Delta\chi(t)$ at $\lambda \simeq 653$ nm (the long-wavelength peak of $\Delta\chi$) also gives a nontrivial dependence of the relaxation time on T_0 (Fig. 16e) with a distinct step (the jump of $\tau_{\Delta\chi}$ in the vicinity of the same point $T_0 = 86$ K) and a subsequent sharp

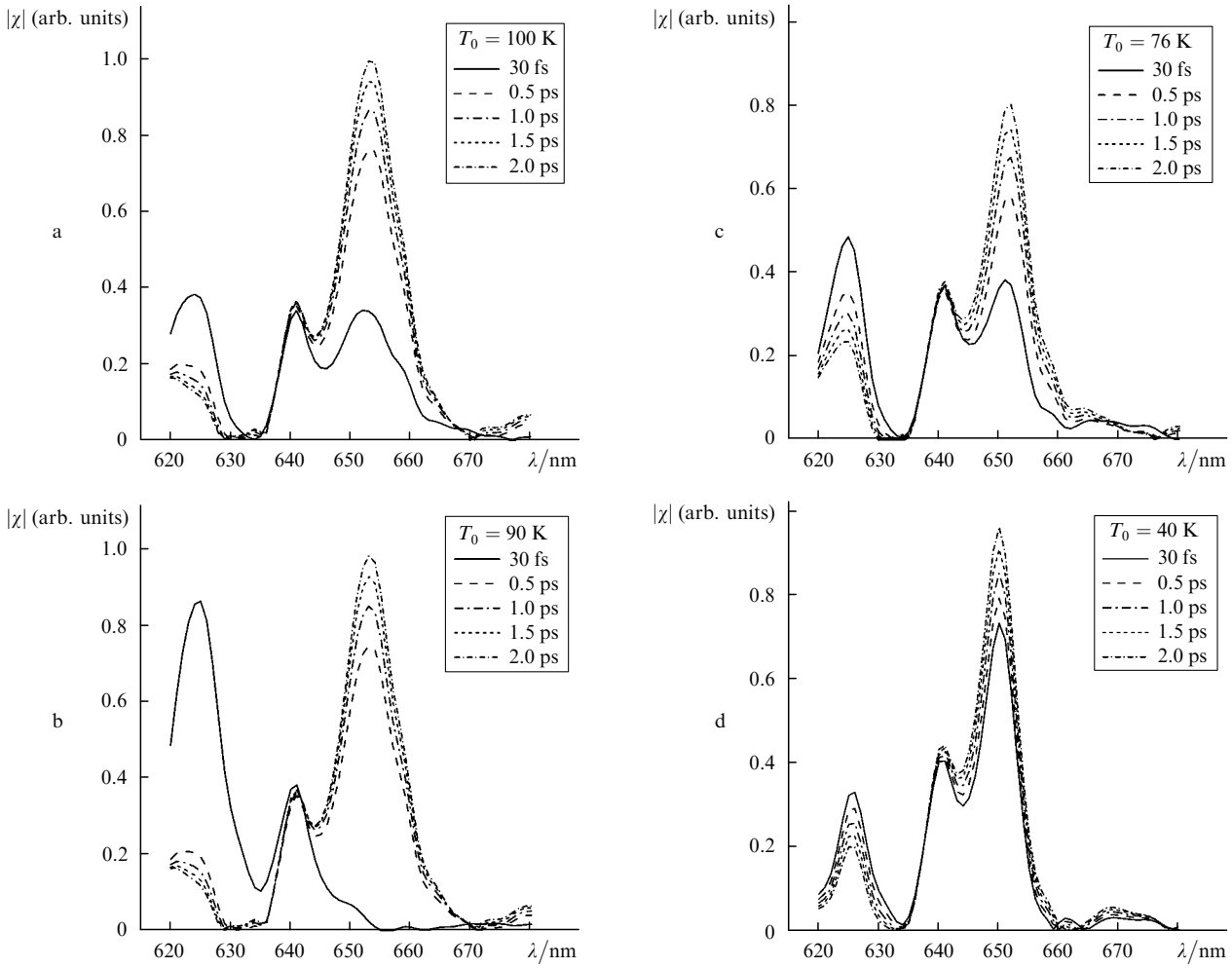

Figure 15. Dependences of the modulus of the response $\chi(\lambda)$ upon two-photon femtosecond probing of the excited state at $T_0 = 100$ (a), 90 (b), 76 (c), and 40 K (d) for different delay times t of the probe pulse.

increase in $\tau_{\Delta\chi}$ in the low-temperature region. Thus, the kinetics of $\Delta\chi(t)$ has the same features as the nonlinear response upon one-photon probing. Note that all these features disappeared completely with decreasing the pump-pulse energy (when $E_{e,h}^F$ and E_0^F coincided).

5.4 Two-photon picosecond pumping – probing

Figure 17 illustrates the calculated transformation of the dependence of the nonresonance component χ_{nr} of the total nonlinear susceptibility χ of the HTSC on the frequency detuning $\Delta\omega$ of the BP components upon varying T_0. Here, variations in the real and imaginary parts of χ_{nr} in the ($\Delta\omega$, T_0) plane are shown at the semi-logarithmic scale (over $\Delta\omega$). It is easy to verify that, due to a reasonable choice of the relaxation rate of the interband polarisation $\Gamma = 150\ \mathrm{cm}^{-1}$ (see section 4), the dependences $\chi_{nr}(\Delta\omega)$ have pronounced spectral features. Also, the jump of χ_{nr} is observed in the vicinity of the point $T_0 \simeq T_c$, which is similar to the jumps shown in Fig. 14 (one-photon picosecond probing).

The resonance component χ_r in the same plane (Fig. 18) behaves considerably simpler. The dependence $\chi_r(\Delta\omega)$ appears upon decreasing the initial temperature T_0 of a sample when the energy gap begins to form (at the point $T_0 = T_c$) and then this dependence follows in fact an increase in the gap width Δ. Note also that because of the finite relaxation rate $\Gamma = 50\ \mathrm{cm}^{-1}$ used in the calculation of χ_r, the contribution of this component proves to be also significant for $\Delta\omega = 0$ (the case of the frequency degeneracy). Therefore, the contribution of χ_r should be also taken into account in the calculation of the total nonlinear response in the DFPS method ($\omega_1 = \omega_2$ for $\boldsymbol{k}_1 \neq \boldsymbol{k}_2$, see below).

For brevity, we do not present here the dependence of the component $\chi_s(\Delta\omega, T_0)$ after the fitting of its complex amplitude χ_{ac} by using the criterion described above. Recall only that all the spectral features of χ_s are unambiguously determined by the spectral width $\delta\omega$ of the BP components, while the temperature parameters are determined by the model itself (see section 4).

Figure 19 shows the dependences of the real and imaginary parts of the total nonlinear susceptibility χ on T_0 and $\Delta\omega$. It is easy to verify that the calculated dependence $\chi(\Delta\omega, T_0)$ preserves all the features of its components considered above. It follows even more clearly from Fig. 20 where the experimental [56] (Fig. 20a) and calculated dependence $\eta(\Delta\omega, T_0) \propto |\chi(\Delta\omega, T_0)|^2$ (Fig. 20b) are presented in the double logarithmic coordinates η and $\Delta\omega$ for the same range of the initial temperature T_0. Taking into account that in fact only two fitting parameters were used in the model – slightly different coincidence points of the BP component frequencies and experimental errors, the agree-

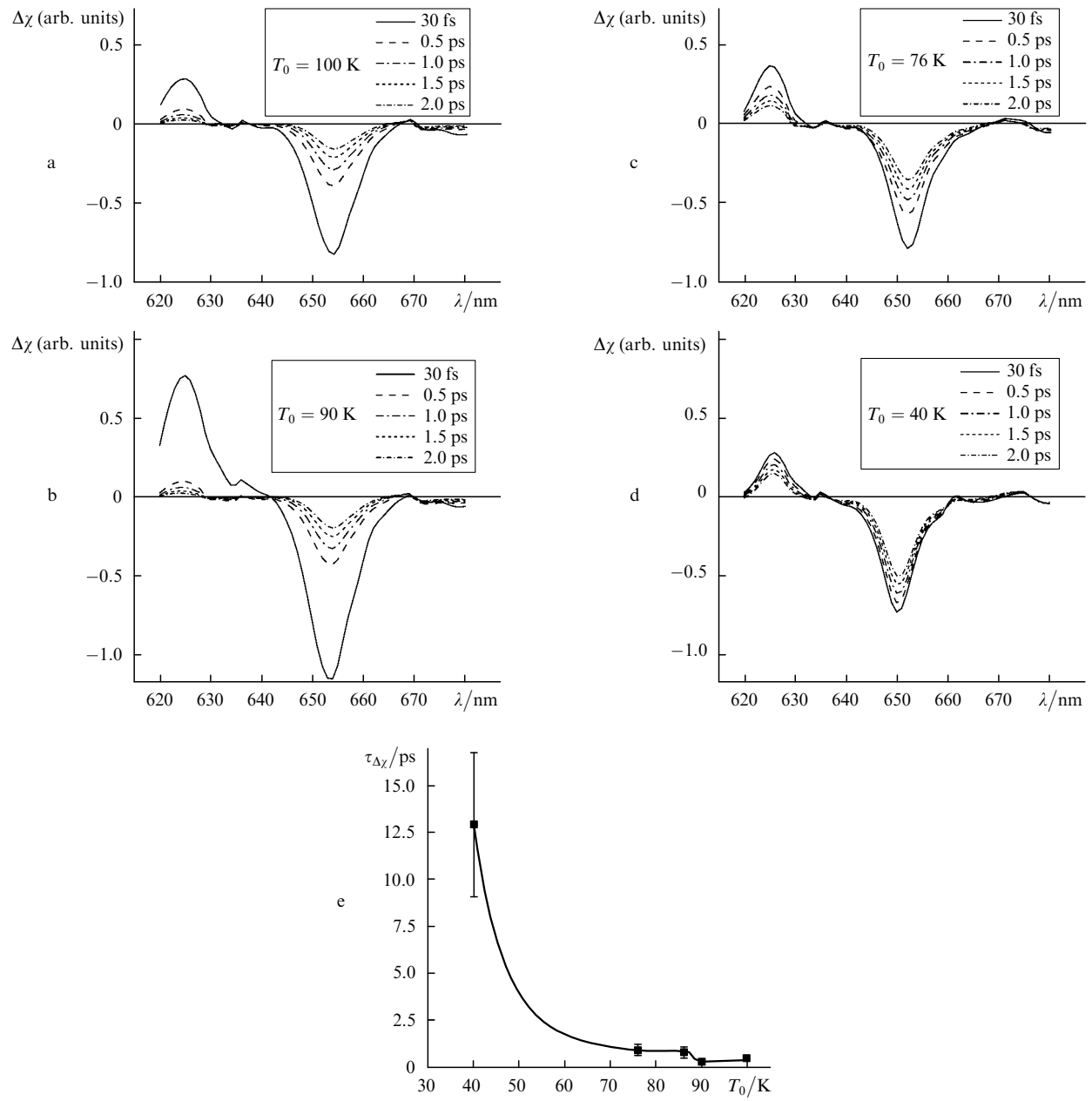

Figure 16. Dependences $\Delta\chi(\lambda)$ upon differential two-photon femtosecond probing for $T_0 = 100$ (a), 90 (b), 76 (c), and 40 K (d) and different delay times t of the probe pulse, and the dependence $\tau_{\Delta\chi}(T_0)$ of the relaxation time of the nonlinear response for probing at 653 nm (e).

ment obtained for the family of the dependences can be considered as satisfactory.

Figure 21 shows at the same double logarithmic scale the calculated transformation of the dependence $\eta(\Delta\omega, T_0)$ upon the shift of the frequency coincidence point ($\Delta\omega = 0$) for the BP components corresponding to wavelengths 625, 630, and 650 nm. One can see that the choice of the point $\Delta\omega = 0$ corresponding to the minimum of the amplitude of the nonresonance component χ_{nr} of the total nonlinear response χ is optimal for revealing the spectral features of its resonance part χ_r and, therefore, for determining the energy-gap parameters.

Figure 22 illustrates the calculated transformation of the dependences of the real and imaginary parts of the nonresonance component χ_{nr} in the frequency-degenerate case ($\omega_1 = \omega_2$ for $\boldsymbol{k}_1 \neq \boldsymbol{k}_2$, the DFPS method). It is easy to verify that due to the consideration of the real band structure of a sample, the dependence $\chi_{nr}(\lambda)$ exhibits distinct spectral features, which weakly depend on the initial temperature T_0 of the sample and are consistent as a whole with experimental data obtained by the pump–probe method and saturation spectroscopy (one-photon probing) [22, 47] and calculations [59–61]. In this case, a characteristic jump of χ_{nr} is also observed in the vicinity of the phase transition temperature $T_0 \sim T_e$. The dependences $\chi_r(T_0)$, $\chi_s(T_0)$, and χ_0 are not presented here because within the framework of the model used for $\Delta\omega = 0$, these components are independent of the picosecond pump–probe wavelength λ.

The behaviour of the total nonlinear response χ (taking into account its components χ_s and χ_0) proves to be substantially different in this case. Figure 23 shows variations in the real and imaginary parts of χ and the experimentally measured dependence of the self-diffraction efficiency $\eta(\lambda, T_0) \propto |\chi(\lambda, T_0)|^2$ in the (λ, T_0) plane. One can

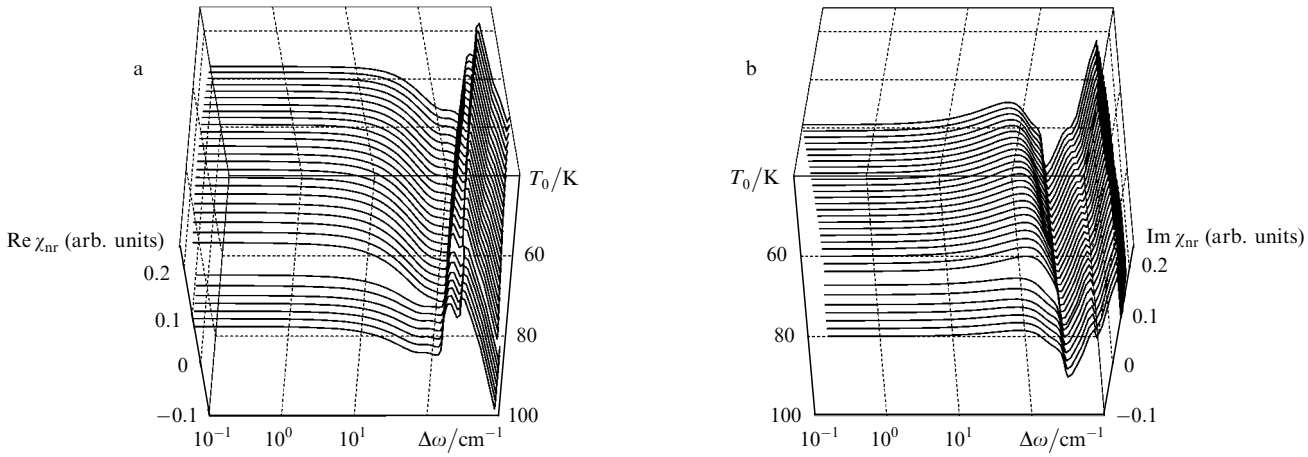

Figure 17. Changes in the real (a) and imaginary (b) parts of χ_{nr} (the BP method) in the ($\Delta\omega$, T_0) plane. The frequency coincidence point $\Delta\omega = 0$ corresponds to $\lambda = 625$ nm. The values of $\Delta\omega$ are plotted at the logarithmic scale.

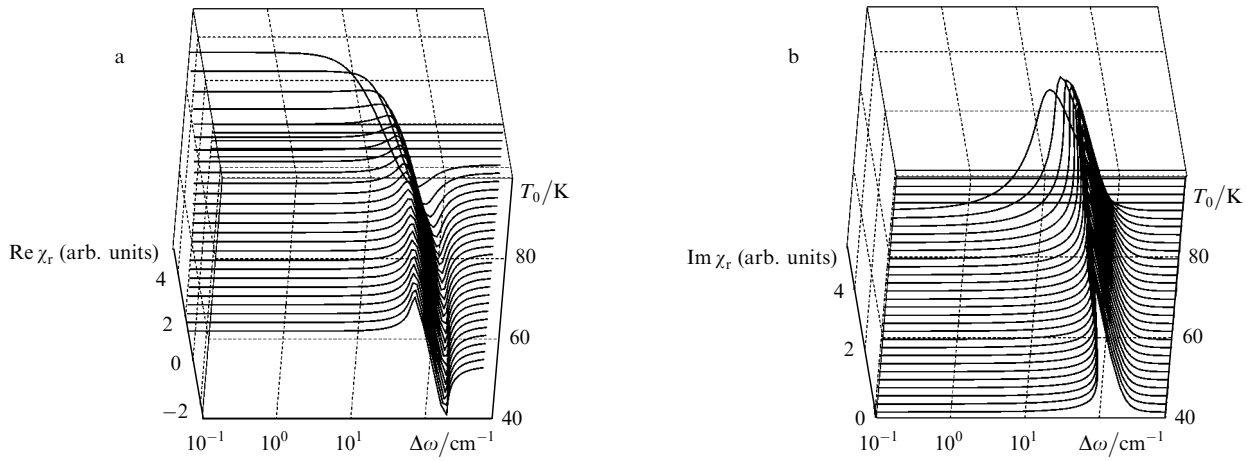

Figure 18. Changes in the real (a) and imaginary (b) parts of χ_r (the BP method) in the ($\Delta\omega$, T_0) plane. The frequency coincidence point $\Delta\omega = 0$ corresponds to $\lambda = 625$ nm. The values of $\Delta\omega$ are plotted at the logarithmic scale.

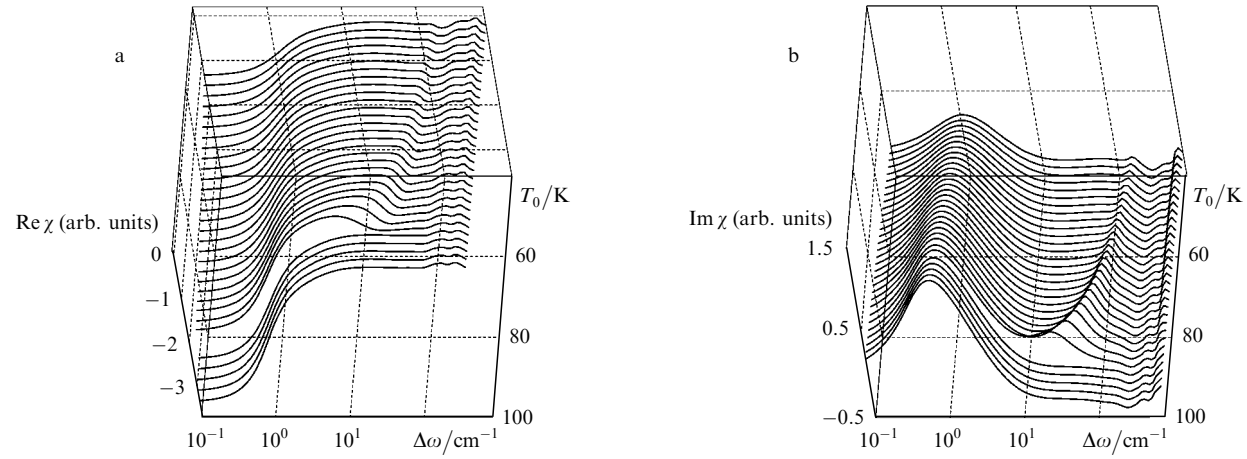

Figure 19. Changes in the real (a) and imaginary (b) parts of χ (the BP method) in the ($\Delta\omega$, T_0) plane. The frequency coincidence point $\Delta\omega = 0$ corresponds to $\lambda = 625$ nm. The values of $\Delta\omega$ are plotted at the logarithmic scale.

see that, while the temperature features of the behaviour of dependences $\chi(\lambda, T_0)$ and $\eta(\lambda, T_0)$ are preserved, their spectral features are inverted, i.e. due to the negative interference of χ_s and χ_{nr}, the positions of maxima and minima on the wavelength axis are interchanged. This means that, in passing from experiments with femtosecond probing of the response kinetics of HTSCs to the two-photon picosecond pump – probe method (efficient excita-

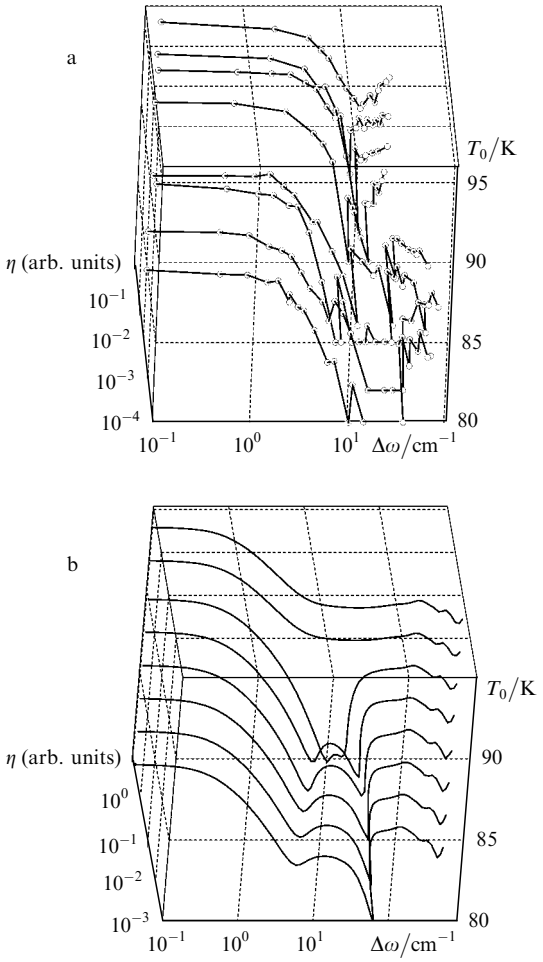

Figure 20. Experimental [56] (a) and calculated (b) dependences $\eta(\Delta\omega, T_0)$ for the BP method. The frequency coincidence point $\Delta\omega = 0$ corresponds to $\lambda = 620.4$ (a) and 625 nm (b). The values of η and $\Delta\omega$ are plotted at the logarithmic scale.

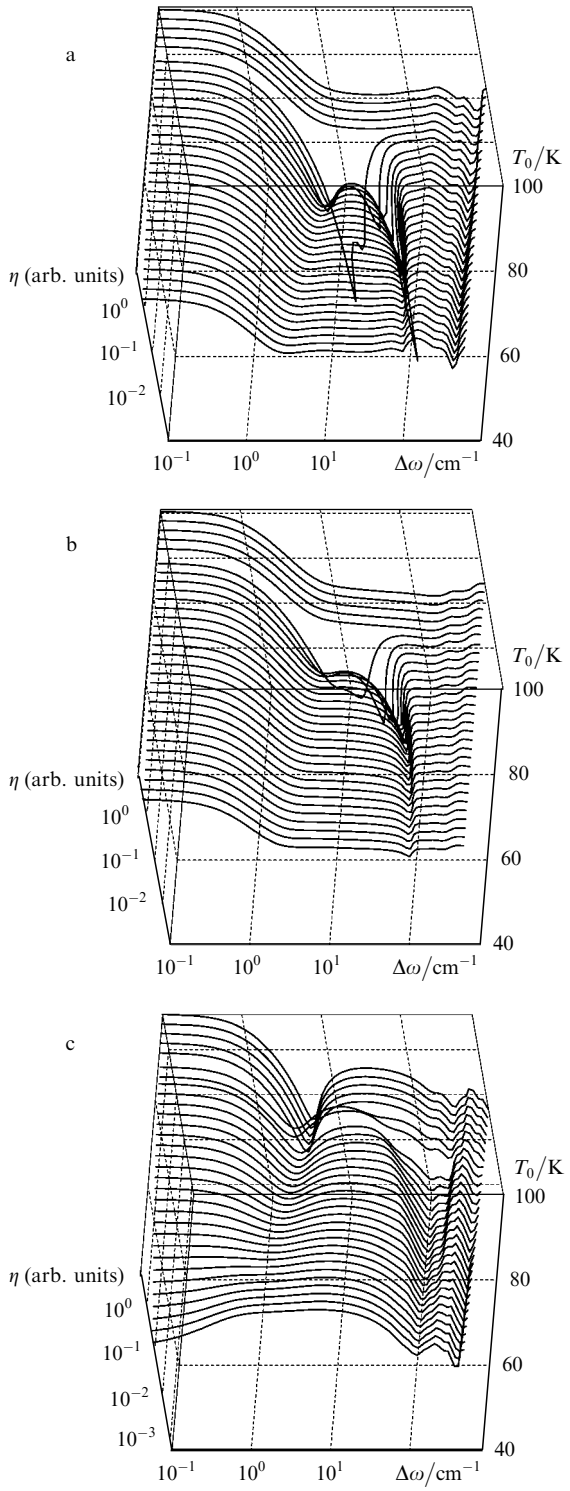

Figure 21. Calculated dependences $\eta(\Delta\omega, T_0)$ for the BP method. The frequency coincidence point $\Delta\omega = 0$ corresponds to $\lambda = 625$ (a), 630 (b), and 650 nm (c). The values of η and $\Delta\omega$ are plotted at the logarithmic scale.

tion of processes involving acoustic phonons), the spectral region of measurements should be shifted.

6. Conclusions

We have shown that almost all spectral, temporal, and temperature features of the nonlinear response of HTSCs, which were observed earlier by various methods of nonlinear spectroscopy, can be interpreted within the framework of the unified and comparatively simple model with a minimal number of fitting parameters. It should be emphasised that this unified model can be used to interpret experiments performed both at high and low levels of pumping by femtosecond [18 – 22, 27, 30 – 34, 47, 48, 52, 53] and picosecond [25, 26, 56] lasers.

The model is based on the consistent consideration of contributions from all possible interband electronic transitions to the dielectric constant ε of a HTSC sample in the real (i.e. known from the literature [100]) electronic spectrum to which a feature simulating the frozen (i.e. metastable [58]) energy gap has been artificially introduced. The metastable nature of the energy gap explains virtually all the features of the nonlinear response of the HTSC, which were observed by various methods of nonlinear spectroscopy at low excitation levels. At the same time, the consideration of the degeneracy, i.e. the shift of the Fermi level for excess free carriers, and the corresponding decrease in the rates of three-body recombination of free carriers allows one to interpret variations in the nonlinear response of the HTSC observed at typical pump-pulse energies $\sim 10^{-7}$ J at the focal spot of diameter 150 μm (high excitation level). The decrease in the recombination

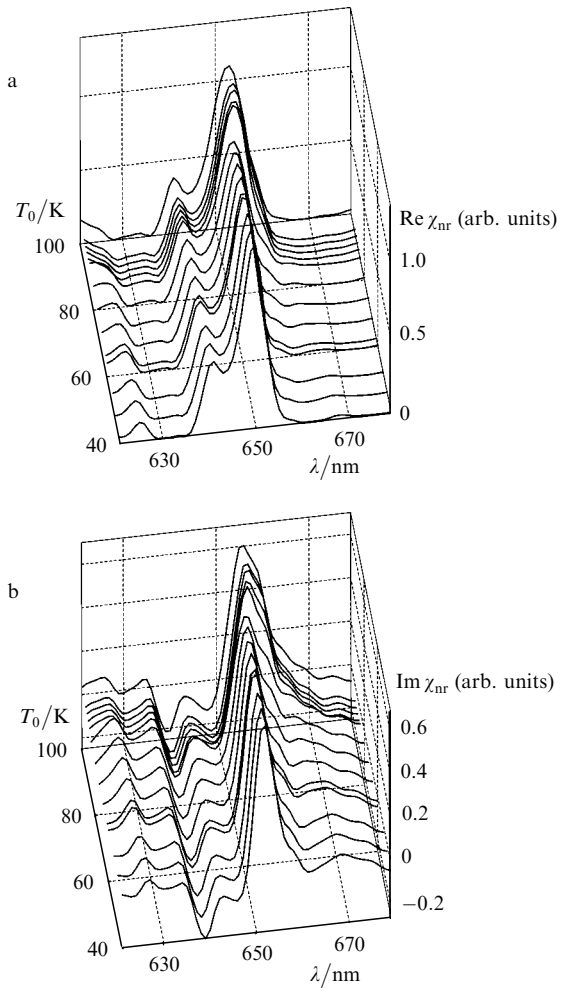

Figure 22. Changes in the real (a) and imaginary (b) parts of the nonresonance component χ_{nr} of the nonlinear response in the DFPS method in the (λ, T_0) plane.

rates $\gamma_{ehp}^{(r)}$ and $\gamma_{ehe}^{(r)}$ required for this is achieved at once after the opening of the energy gap in the electronic spectrum of the HTSC (the decrease in the initial temperature T_0 of the HTSC sample slightly below the phase transition temperature T_c) due to the unusual shape (compared to the electronic spectrum of narrow-gap semiconductors) of the electronic state density function $g(E_e)$.

Note that so far the predictions of models used for interpreting experimental data could explain only one of the experiments, contradicting inevitably the results of other measurements.

References

1. Rosei R. et al. *Phys. Rev. B*, **10**, 484 (1974).
2. Eesley G.L. *Phys. Rev. Lett.*, **51**, 2140 (1983).
3. Elsayed-Ali H.E. et al. *Phys. Rev. Lett.*, **58**, 1212 (1987).
4. Schoenlein R.W. et al. *Phys. Rev. Lett.*, **58**, 1680 (1987).
5. Fann W.S. et al. *Phys. Rev. B*, **46**, 13592 (1992).
6. Sun C.K. et al. *Phys. Rev. B*, **48**, 12365 (1993).
7. Groeneveld R.H.M. et al. *Phys. Rev. B*, **51**, 11433 (1995).
8. Dobryakov A.L. et al. *Physica Scripta*, **60**, 572 (1999).
9. Petnikova V.M. et al. *Kvantovaya Elektron.*, **28**, 69 (1999) [*Quantum Electron.*, **29**, 626 (1999)].
10. Kuznetsova L.P. et al. *Kvantovaya Elektron.*, **30**, 175 (2000) [*Quantum Electron.*, **30**, 175 (2000)].

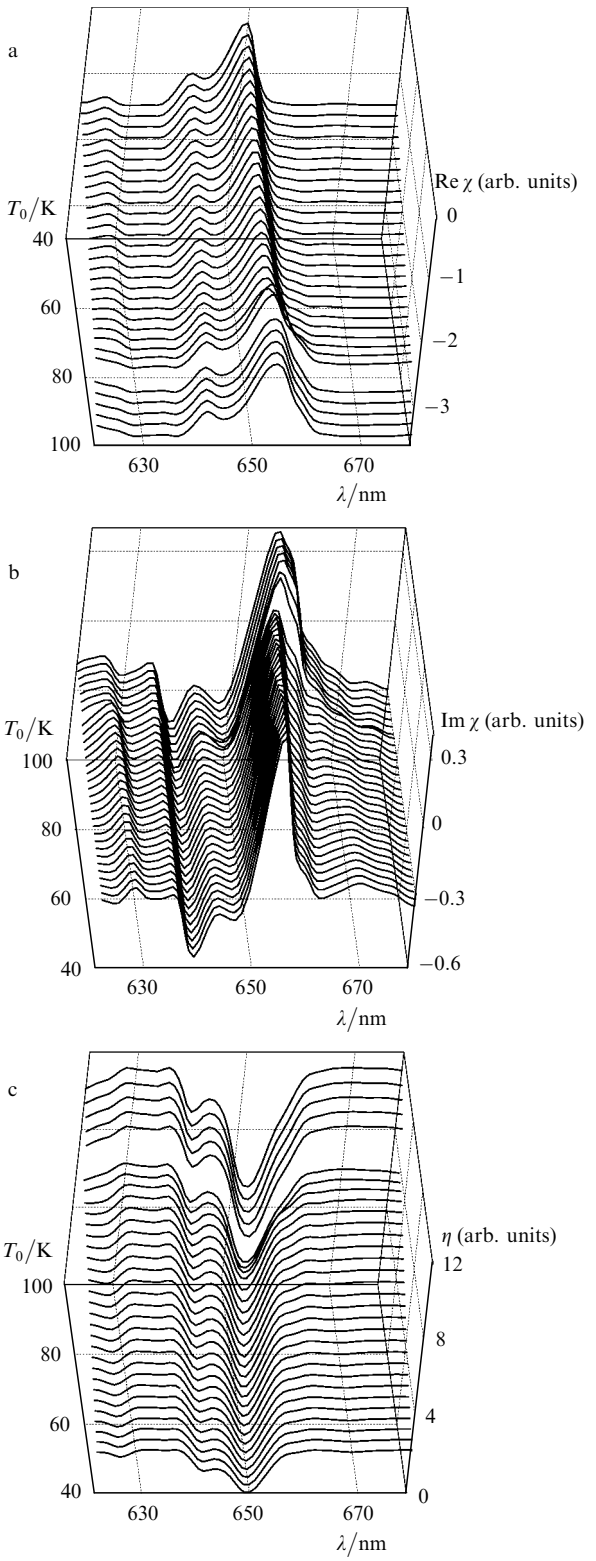

Figure 23. Changes in the real (a) and imaginary (b) parts of the total nonlinear response χ and the self-diffraction efficiency η (c) in the DFPS method in the (λ, T_0) plane.

11. Bobyrev Yu.V. *Kvantovaya Elektron.*, **32**, 789 (2002) [*Quantum Electron.*, **32**, 789 (2002)].
12. Rothwarf A., Taylor B.N. *Phys. Rev. Lett.*, **19**, 27 (1967).
13. Owen C.S., Scalapino D.J. *Phys. Rev. Lett.*, **28**, 1559 (1972).
14. Parker W.H., Williams W.D. *Phys. Rev. Lett.*, **29**, 924 (1972).
15. Schuller I., Gray K.E. *Phys. Rev. Lett.*, **36**, 429 (1976).
16. Bluzer N.J. *Appl. Phys.*, **71**, 1336 (1992).

17. Forrester M.G. *Appl. Phys. Lett.*, **53**, 1332 (1988).
18. Brorson S.D. et al. *Phys. Rev. Lett.*, **64**, 2172 (1990).
19. Han S.G. et al. *Phys. Rev. Lett.*, **65**, 2708 (1990).
20. Gershenzon M.E. et al. *Pis'ma Zh. Eksp. Ter. Fiz.*, **52**, 1189 (1990).
21. Kazeroonian A.S. et al. *Solid State Commun.*, **78**, 95 (1991).
22. Chekalin S.V. et al. *Phys. Rev. Lett.*, **67**, 3860 (1991).
23. Bluzer N. *Phys. Rev. B*, **44**, 10222 (1991).
24. Hegman F.A. et al. *Appl. Phys. Lett.*, **62**, 1158 (1993).
25. Zherikhin A.N. et al. *Physica C*, **221**, 311 (1994).
26. Zherikhin A.N. et al. *Kvantovaya Elektron.*, **21**, 574 (1994) [*Quantum Electron.*, **24**, 529 (1994)].
27. Brorson S.D. et al. *Phys. Rev. B*, **49**, 6185 (1994).
28. Buhleier R. et al. *Phys. Rev. B*, **50**, 9672 (1994).
29. White J.O. et al. *Physica C*, **235–240**, 2025 (1994).
30. Stevens C.J. et al. *Phys. Rev. Lett.*, **78**, 2212 (1997).
31. Smith D.C. et al. *J. Low Temperature Physics*, **117**, 1059 (1999).
32. Demsar J. et al. *Phys. Rev. B*, **63**, 054519 (2001).
33. Segre G.P. et al. *Phys. Rev. Lett.*, **88**, 137001 (2002).
34. Schneider M.L. et al. *Eur. Phys. J. B*, **36**, 327 (2003).
35. Voronov A.V. *Kvantovaya Elektron.*, **31**, 1058 (2001) [*Quantum Electron.*, **31**, 1058 (2001)].
36. Bobyrev Yu.V. et al. *Kvantovaya Elektron.*, **31**, 1067 (2001) [*Quantum Electron.*, **31**, 1067 (2001)].
37. Bobyrev Yu.V. et al. *Kvantovaya Elektron.*, **33**, 998 (2003) [*Quantum Electron.*, **33**, 998 (2003)].
38. Allen P.B. *Phys. Rev. Lett.*, **59**, 1460 (1987).
39. Nessler W. et al. *Phys. Rev. Lett.*, **81**, 4480 (1998).
40. Sun C.K. et al. *Phys. Rev. B*, **50**, 15337 (1994).
41. Demsar J. xxx.lanl.gov/archive/cond-mat/0305597 (2003).
42. Kaganov M.I. et al. *Zh. Eksp. Teor. Fiz.*, **31**, 242 (1956).
43. Haberland P.H., Shiffman C.A. *Phys. Rev. Lett.*, **19**, 1337 (1967).
44. Gantmakher V.F., Leonov Yu.S. *Pis'ma Zh. Eksp. Teor. Fiz.*, **8**, 264 (1968).
45. Bradfield J.E., Coon J.B. *Phys. Rev. B*, **7**, 5072 (1973).
46. Tinkham M., Clarke J. *Phys. Rev. Lett.*, **28**, 1366 (1972).
47. Farztdinov V.M. et al. *Brazilian J. Phys.*, **26**, 482 (1996).
48. Kabanov V.V. et al. *Phys. Rev. B*, **61**, 1477 (2000).
49. Lucas G., Stephen M.J. *Phys. Rev.*, **154**, 349 (1967).
50. Woo J.W.F., Abrahams E. *Phys. Rev.*, **169**, 407 (1968).
51. Schmid A., Schoen G. *J. Low Temperature Phys.*, **20**, 207 (1975).
52. Kabanov V.V. et al. *Phys. Rev. B*, **59**, 1497 (1999).
53. Schneider M.L. et al. *Europhys. Lett.*, **60**, 460 (2002).
54. Bonn D.A. et al. *Phys. Rev. B*, **47**, 11314 (1993).
55. Quinlan S.M. et al. *Phys. Rev. B*, **49**, 1470 (1994).
56. Zherikhin A.N. et al. *Phys. Lett. A*, **179**, 145 (1993).
57. Grishanin B.A. et al. *Laser Phys.*, **3**, 121 (1993).
58. Voronov A.V. *Zh. Eksp. Teor. Fiz.*, **120**, 1256 (2001).
59. Bobyrev Yu.V. et al. *Kvantovaya Elektron.*, **35**, 720 (2005) [*Quantum Electron.*, **35**, 720 (2005)].
60. Bobyrev Yu.V. et al. *Kvantovaya Elektron.*, **35**, 729 (2005) [*Quantum Electron.*, **35**, 729 (2005)].
61. Bobyrev Yu.V. et al. *Kvantovaya Elektron.*, **35**, 1039 (2005) [*Quantum Electron.*, **35**, 1039 (2005)].
62. Farztdinov V.M. et al. *Phys. Rev. B*, **56**, 4176 (1997).
63. Lozovik Yu.E. et al. *Laser Phys.*, **9**, 557 (1999).
64. Kuznetsova L.P. et al. *J. Raman Spectroscopy*, **31**, 755 (2000).
65. Devos A., Lerouge C. *Phys. Rev. Lett.*, **86**, 2669 (2001).
66. Kornienko A.G. et al. *J. Appl. Phys.*, **80**, 2396 (1996).
67. Bobyrev Yu.V. et al. *Kvantovaya Elektron.*, **35**, 102 (2005) [*Quantum Electron.*, **35**, 102 (2005)].
68. Fujimori A. et al. *Solid State Commun.*, **63**, 857 (1987).
69. Schlesinger Z. et al. *Physica C*, **185–189**, pt.1, 57 (1991).
70. Fink J. et al. *J. Electron Spectroscopy and Related Phenomena*, **66**, 395 (1994).
71. Birgeneau R.J., Shirane G., in *Physical Properties of High Temperature Superconductors I* (Singapore: World Scientific, 1989) p. 151.
72. Rossat-Mignod J. et al. *Physica C*, **185–189**, pt.1, 86 (1991); Tranquada J.M. et al. *Phys. Rev. B*, **46**, 5561 (1992).
73. Shirane G. *Physica C*, **185–189**, pt.1, 80 (1991).
74. Kastner M.A. et al. *Phys. Rev. B*, **38**, 6636 (1988).
75. Ginzburg V.L., Kirzhnits D.A. (Eds) *Problemy vysokotemperasturnoi provodimosti* (Problems of High-Temperature Superconductivity) (Moscow: Nauka, 1977).
76. Annett J.F. et al. *J. Low Temperature Phys.*, **105**, 473 (1996).
77. Moreo A. et al. *J. Phys. Chem. Sol.*, **56**, 1645 (1995).
78. Norman M.R. et al. *Nature*, **392**, 157 (1998).
79. Demsar J. et al. *Phys. Rev. Lett.*, **82**, 4918 (1999).
80. Cohn J.L., Karpinski J. *Phys. Rev. B*, **58**, 14617 (1988).
81. Tranquada J.M. et al. *Nature*, **375**, 561 (1995).
82. Buchner B. et al. *Phys. Rev. Lett.*, **73**, 1841 (1994).
83. Baskaran G. et al. *Solid State Commun.*, **63**, 973 (1987).
84. Putikka W.O. et al. *Phys. Rev. Lett.*, **68**, 538 (1992).
85. Dagotto E. *Rev. Modern Phys.*, **66**, 763 (1994).
86. Hybertsen M.S. et al. *Phys. Rev. B*, **41**, 11068 (1990).
87. Yonemitsu K. et al. *Phys. Rev. B*, **47**, 12059 (1993).
88. Binder K. (Ed.) *Monte Carlo Methods in Statistical Physics* (Berlin: Springer, 1986).
89. Shraiman B.I., Siggia E.D. *Phys. Rev. B*, **40**, 9162 (1989).
90. Frenkel D.M., Hanke W. *Phys. Rev. B*, **42**, 6711 (1990).
91. Stojkovic B.P. et al. xxx.lanl.gov/archive/cond-mat/9911380 (1999).
92. Landau L.D., Lifshits E.M. *Statistical Physics* (Oxford: Pergamon Press, 1980; Moscow: Nauka, 1995).
93. Animalu A. *Intermediate Quantum Theory of Crystalline Solids* (Prentice-Hall, Englewood Cliffs, 1977; Moscow: Mir, 1981).
94. Korn G.A., Korn T.M. *Mathematical Handbook for Scientists and Engineers* (New York: McGraw-Hill, 1961; Moscow: Nauka, 1971).
95. Nelder J.A., Mead R. *Computer J.*, **7**, 308 (1965).
96. Lifshits E.M., Pitaevskii L.P. *Physical Kinetics* (Oxford: Pergamon Press, 1981; Moscow: Nauka, 1979).
97. Rozanov N.N. *Opticheskaya bistabil'nost' i gisteresis v raspredelennykh nelineinykh sistemakh* (Optical Bistability and Hysteresis in Distributed Nonlinear Systems) (Moscow: Nauka, 1997).
98. Vasil'ev V.A. et al. *Avtovolnovye protsessy* (Autowave Processes) (Moscow: Nauka, 1987).
99. Abakumov V.N. et al. *Bezyzluchatel'nya rekombinatsiya v poluprovodnikakh* (Nonradiative Recombination in Semiconductors) (St. Petersburg: St. Petersburg Institute of Nuclear Physics, 1997).
100. Perry J.K. et al. *Phys. Rev. B*, **63**, 144501 (2001).
101. Chadi D.J., Cohen M.L. *Phys. Rev. B*, **8**, 5747 (1973).
102. Schubert M., Wilhelmi B. *Nonlinear Optics and Quantum Electronics* (New York: Wiley, 1986).
103. Apanasevich P.A. *Osnovy vzaimodeistviya sveta s veshchestvom* (Fundamentals of the Interaction of Light with Matter) (Minsk: Nauka i Tekhnika, 1977).
104. Akhmanov S.A., Koroteev N.I. *Metody nelineinoi optiki v spektroskopii rasseyaniya sveta* (Methods of Nonlinear Optics in Light Scattering Spectroscopy) (Moscow: Nauka, 1981).
105. Koroteev N.I. *Vestn. Mosk. Univ., Ser. Fiz. Astron.*, (6), 6 (1996).